

RESEARCH

Open Access



# Microglia-targeting nanosystems that cooperatively deliver Chinese herbal ingredients alleviate behavioral and cognitive deficits in Alzheimer's disease model mice

Peng Zhou<sup>1</sup>, Quan Chao<sup>1</sup>, Chen Li<sup>1</sup>, Ningjing Wang<sup>1</sup>, Siqi Guo<sup>1</sup>, Pingping Wang<sup>1</sup>, Pingyuan Ge<sup>1</sup>, Caihong Li<sup>1</sup>, Rui Guo<sup>1</sup>, Nianyun Yang<sup>1</sup>, Zhangdi Lu<sup>4</sup>, Zhishu Tang<sup>2,3</sup>, Qichun Zhang<sup>1</sup>, Tingming Fu<sup>1</sup>, Qingqing Xiao<sup>1\*</sup> and Huaxu Zhu<sup>1\*</sup>

## Abstract

The effective treatment of Alzheimer's disease (AD) is challenging because of its complex and controversial pathological mechanisms. Moreover, multiple barriers, such as the blood–brain barrier (BBB), reduce drug delivery efficiency. Microglia-related neuroinflammation has recently attracted increasing attention as a possible cause of AD and has become a novel therapeutic target. Therefore, overcoming the BBB and targeted delivery of anti-inflammatory agents to microglia seem to be effective practical strategies for treating AD. A large proportion of natural active extracts possess exceptional immunomodulating capabilities. In this study, the cooperative delivery of berberine (Ber) and palmatine (Pal) by transferrin-decorated extracellular vesicles (Tf-hEVs-Ber/Pal), which can cross the BBB and precisely target microglia, was performed. This nanosystem effectively cleared amyloid  $\beta$ -protein ( $A\beta$ ) aggregates, significantly regulated the neuroinflammatory environment both in vitro and in vivo and markedly altered the behavior and improved the cognitive and learning abilities of AD model mice. The efficacy of a microglia-targeting combined therapeutic approach for AD was demonstrated, which broadens the potential application of Chinese herbal ingredients.

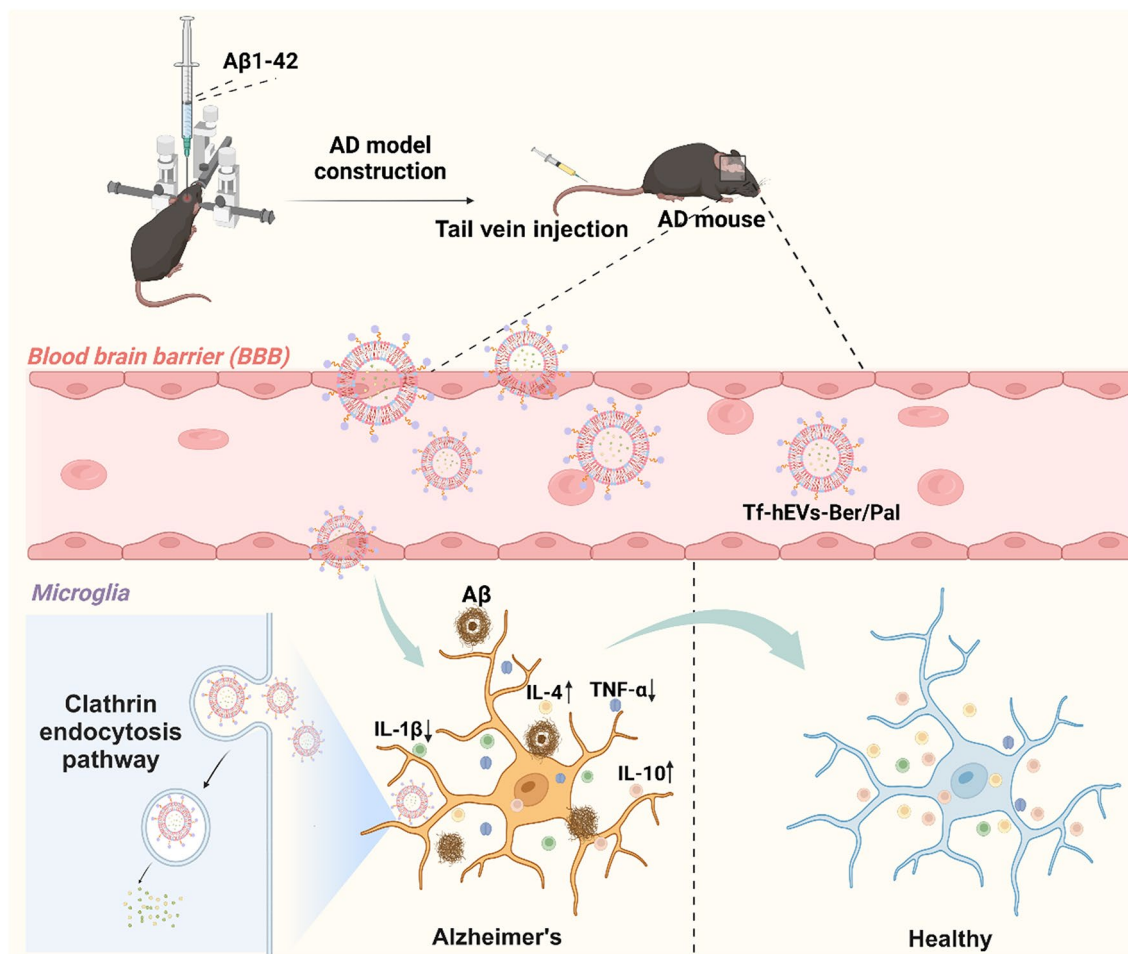
\*Correspondence:

Qingqing Xiao  
xiaoqq@njucm.edu.cn  
Huaxu Zhu  
zhuhx@njucm.edu.cn

Full list of author information is available at the end of the article



© The Author(s) 2025. **Open Access** This article is licensed under a Creative Commons Attribution-NonCommercial-NoDerivatives 4.0 International License, which permits any non-commercial use, sharing, distribution and reproduction in any medium or format, as long as you give appropriate credit to the original author(s) and the source, provide a link to the Creative Commons licence, and indicate if you modified the licensed material. You do not have permission under this licence to share adapted material derived from this article or parts of it. The images or other third party material in this article are included in the article's Creative Commons licence, unless indicated otherwise in a credit line to the material. If material is not included in the article's Creative Commons licence and your intended use is not permitted by statutory regulation or exceeds the permitted use, you will need to obtain permission directly from the copyright holder. To view a copy of this licence, visit <http://creativecommons.org/licenses/by-nc-nd/4.0/>.

**Graphical abstract**

**Keywords** Targeting nanosystems, Chinese herbal medicines, Alzheimer's disease, Neuroinflammation, Microglia phenotype

**Introduction**

Microglia, crucial resident immune cells in the brain, have a range of diverse functions related to brain processes. Therefore, pathological changes in the metabolism and phenotype of microglia can gradually lead to severe cerebral diseases, such as Alzheimer's disease (AD) and Parkinson's disease [1, 2]. Recently, microglial inflammation has been reported as a potential pathogenic factor in AD [3]. When stimulated by various inflammatory signals, such as lipopolysaccharide (LPS) and amyloid  $\beta$  (A $\beta$ ), the intracellular metabolism of microglia is reprogrammed, characterized by an increase in glycolysis, upregulation of hypoxia-inducible factor 1 alpha (HIF-1 $\alpha$ ) and enhancement of rapamycin (mTOR) transcription, disruption of the tricarboxylic acid (TCA) cycle in the mitochondria, and a decrease in oxidative phosphorylation. Various proinflammatory factors,

such as nitric oxide (NO), interleukin 1 beta (IL-1 $\beta$ ) and tumor necrosis factor alpha (TNF- $\alpha$ ), are produced and secreted, resulting in neuroinflammation and ultimately causing significant cognitive decline [4]. Moreover, a clinical study analyzed the mononuclear transcriptome and epigenome of approximately 194,000 microglia from 443 AD patients and revealed that with the progression of AD, more microglia enter the inflammatory state, leading to uncontrollable neuroinflammation and exacerbating central nervous system dysfunction [5]. Transforming microglia from the proinflammatory phenotype to the anti-inflammatory, phagocytic phenotype may improve neuronal function and serve as an effective strategy for the treatment of AD.

Berberine (Ber) and palmatine (Pal), which are natural alkaloids extracted from the Chinese herb *Coptis chinensis* Franch., have been reported to have multifarious

pharmacological properties, including anti-inflammatory, antioxidative, immunomodulatory, cardio-cerebrovascular protective, and hepatoprotective properties [6, 7]. Interestingly, we screened four anti-inflammatory components derived from *Coptis chinensis*, and the synergistic effect between these two components was reported in our previous work. However, the abilities of Ber and Pal to cross the blood-brain barrier (BBB) and target the brain are poor. In particular, the BBB limits the passage and transport of more than 98% of small molecules and macromolecular therapeutics into the brain [8]. Nanoparticle-mediated drug delivery systems are crucial for targeted treatment because they can overcome the limitations of free drugs and enhance their brain-targeting performance [9–11].

Exosomes (Exos) are naturally derived vesicles with sizes ranging from 30 nm to 150 nm, offering advantages such as biocompatibility and a “homing effect” [12]. Unfortunately, its progressive application has been limited by the extraction process and batch-to-batch stability [13–15]. Liposomes (Lips) are synthetic vesicles composed of phospholipids and cholesterol, with sizes ranging from 20 nm to 200 nm. They offer various benefits, including biocompatibility, ease of decoration to improve their targeting ability, and a well-established preparation process [16–19]. The above two nanosystems have similar structures; both contain hydrophilic cores and a lipid bilayer, and active membrane fusion is a prominent feature of phospholipid bilayer membranes [20–27]. Accordingly, hybrid nanoextracellular vesicles (hEVs) were prepared by fusing microglia-derived Exos and artificial Lips, which naturally integrate the characteristics and advantages of both and compensate for each other's limitations. Transferrin (Tf) is a widely utilized ligand that can specifically interact with transferrin receptors (TfRs), which are upregulated in the endothelial cells of the BBB in the context of brain disorders. Tf was employed to modify hEVs, and Tf-hEVs were prepared to facilitate specific transport across the BBB and enable the drugs to target the brain by leveraging the high-affinity binding of Tf to TfRs [28].

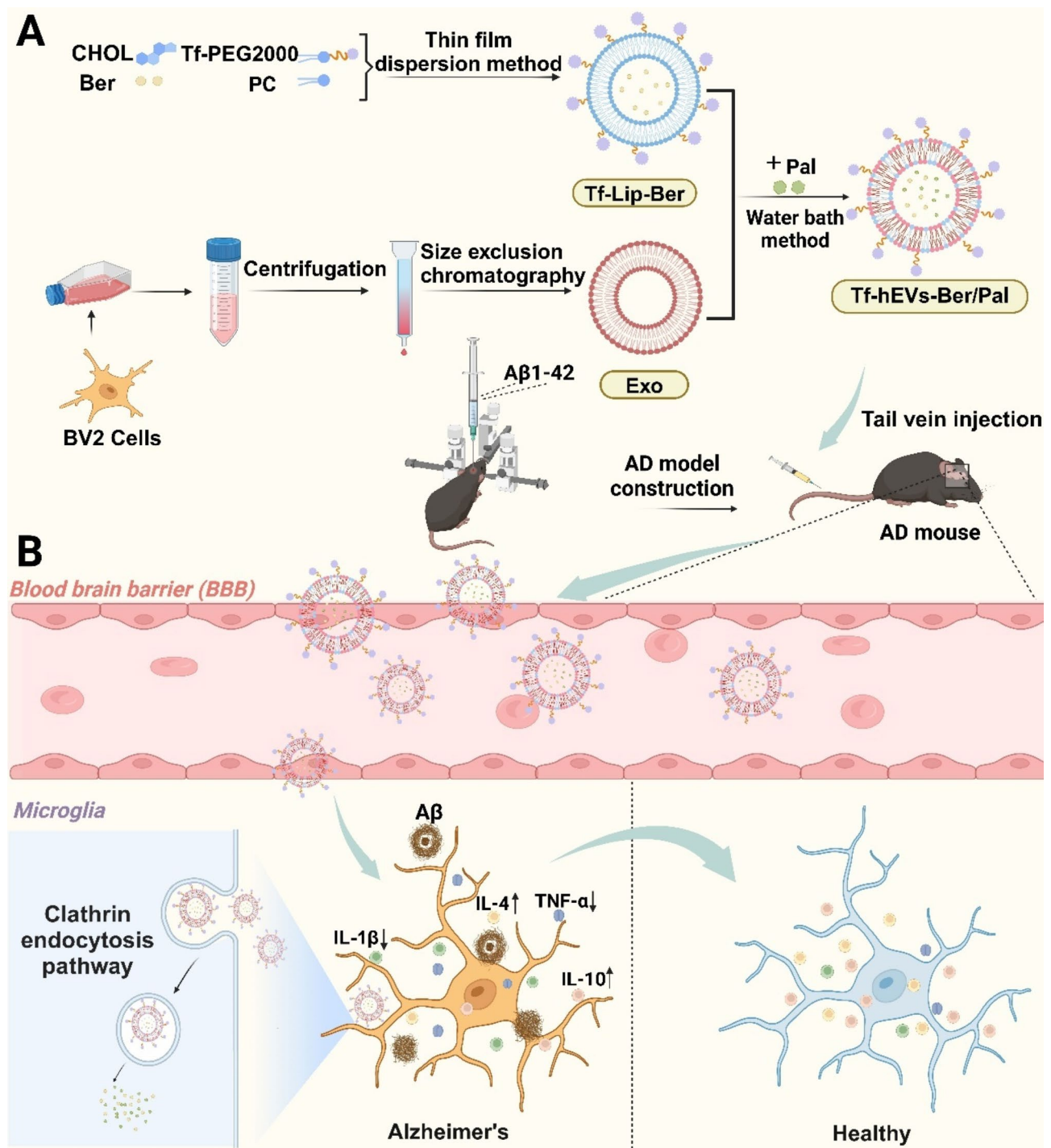
Inspired by the above background information, a hybrid vesicle consisting of microglia-derived Exos and Tf-modified liposomes cooperatively loaded with Ber and Pal (Tf-hEVs-Ber/Pal) was prepared for AD treatment (Scheme 1). Tf-hEVs-Ber/Pal could cross the BBB and further target microglia with the assistance of Tf modification and the homing effect of Exos. The nanosystems subsequently efficiently delivered Ber and Pal into the brain, significantly improving the behavioral and cognitive functions of AD model mice. They also enhanced the clearance of A $\beta$  aggregates and promoted the transformation of microglia to an anti-inflammatory phenotype. Additionally, the nanosystems effectively balanced

inflammatory responses by increasing anti-inflammatory cytokine levels and suppressing proinflammatory signals both in vitro in microglia and in vivo in the hippocampal region. Here, we proposed a novel nanobiotechnology for the treatment of brain disorders that has broad application prospects and expanded the utility of active Chinese herbal medicines.

## Materials and methods

### Materials

Hydrogenated soybean phosphatidylcholine (HSPC) and cholesterol (CHOL) were purchased from Shanghai Advanced Vehicle Technology Pharmaceutical Co., Ltd. (Shanghai, China). Tf-mPEG2000 was purchased from Xi'an Ruixi Biotechnology Co., Ltd. (Xi'an, China). Ber and Pal were purchased from Macklin (Chengdu, China). A $\beta$ 1–42 was obtained from Shanghai Nuo Biotechnology Co., Ltd. (Shanghai, China). Fluorescein isothiocyanate (FITC) was obtained from Shanghai Aladdin Biochemical Technology Co., Ltd. (Shanghai, China). 4',6-Diamidindine 2-phenylindole (DAPI) was purchased from Solarbio Technologies, Inc. 1,1'-Dioctadecyl-3,3,3',3'-tetramethylindotricarbocyanine iodide (DiR), 1,1'-dioctadecyl-3,3,3',3'-tetramethylindocarbocyanine perchlorate (DiL), 1,1'-dioctadecyl-3,3,3',3'-tetramethylindodicarbocyanine, 4-chlorobenzenesulfonate salt (DiD). 2-(4-Amidinophenyl)-6-indolecarbamide dihydrochloride (DAPI), LysoTracker Red, and a BCA protein assay kit were purchased from Shanghai Beyotime Biotechnology (Shanghai, China). Colchicine, nystatin, beta-cyclodextrin, and chlorpromazine were purchased from Beijing Pusitang Biotechnology Co., Ltd. (Beijing, China). An anti-CD81 monoclonal antibody, anti-Alix polyclonal antibody, anti-TSG101 polyclonal antibody, AlexaFluor 647 conjugated-goat anti-rabbit recombinant secondary antibody, and anti-CD71 recombinant antibody were purchased from Wuhan Sanying Biotechnology Co., Ltd. (Wuhan, China). ELISA kits for TNF- $\alpha$ , IL-1 $\beta$ , IL-4, IL-10, A $\beta$ 40, and A $\beta$ 42 were obtained from Shanghai Enzyme Linked Biotechnology Co., Ltd. (Shanghai, China). Biochemical assay kits for alanine aminotransferase (ALT), aspartate aminotransferase (AST), albumin (ALB), total protein (TP), creatinine (CREA), and blood urea nitrogen (BUN) were obtained from Rayto Life and Analytical Sciences Co., Ltd. (Shenzhen, China). BV2 cells, the brain endothelial cell line bEND.3 (bEND.3 cells) and human embryonic kidney 293 cells (HEK293) were purchased from the National Biomedical Cell-Line Resource Center (Beijing, China). SPF male C57BL/6J mice (6–8 weeks old), weighing 20  $\pm$  3 g, were purchased from Jiangsu Huachuang Senuo Medical Technology Co., Ltd.



**Scheme 1** Preparation of the microglia-targeting nanosystem Tf-hEVs-Ber/Pal and its possible mechanism. **(A)** Tf-Lip-Ber was prepared by the thin film dispersion method, and Exos were extracted from microglia (BV2 cells) simultaneously. Subsequently, Tf-Lip-Ber, Exo, and Pal were mixed and fused via the water bath method to obtain Tf-hEVs-Ber/Pal. **(B)** A $\beta$  protein was injected into the hippocampi of C57BL/6J mice to establish an AD mouse model. Tf-hEVs-Ber/Pal were injected via the tail vein, circulated in the blood, targeted the blood–brain barrier via the Tf/TfR interaction, and then targeted microglia through the homing effect of the Exo membrane via the clathrin-mediated pathway. After Tf-hEVs-Ber/Pal treatment, the number of A $\beta$  plaques and the levels of proinflammatory cytokines (TNF- $\alpha$  and IL-1 $\beta$ ) were decreased, and the levels of anti-inflammatory cytokines (IL-4 and IL-10) were increased, thereby restoring the spatial learning ability and cognitive function of AD model mice

### Extraction and identification of exosomes

Microglia Exos were extracted by size exclusion chromatography. In brief, BV2 cells were seeded in T25 culture flasks and cultured in high-glucose DMEM containing 10% fetal bovine serum (FBS) in a humidified incubator at 37 °C with 5% CO<sub>2</sub>. When the cell density reached 60%, the medium was replaced with exosome-depleted medium prepared with 10% exosome-free FBS. Once the cells reached confluence, the supernatant was collected. The supernatant was subjected to gradient centrifugation to remove cell debris and large particles, followed by filtration using a 100 kDa ultrafiltration tube to obtain pretreated samples. The pretreated sample was then slowly loaded onto the chromatography column, and Exos were eluted and collected with gently flowing elution buffer. The size distribution, zeta potential and polydispersity index (PDI) of the Exo particles were measured by dynamic light scattering (DLS) and observed with a transmission electron microscopy (TEM).

The signature membrane proteins were analyzed by western blotting (WB). Briefly, Exo samples were lysed in radioimmunoprecipitation assay (RIPA) buffer, and protein concentrations were determined using a BCA kit. A 25 µg aliquot of protein was separated by sodium dodecyl sulfate–polyacrylamide gel electrophoresis (SDS–PAGE) and transferred onto a nitrocellulose (NC) membrane. The membrane was blocked with 5% skim milk for 2 h, followed by three washes with TBST (Tris-buffered saline with Tween-20). The membrane was incubated overnight at 4 °C with the following primary antibodies: anti-rabbit TSG101, anti-rabbit CD81, and anti-rabbit CD26. The following day, the membrane was incubated with HRP-conjugated anti-rabbit IgG secondary antibodies at room temperature for 1 h, followed by washing with TBST. Bands were visualized using the ECL Prime western blotting system (GE Healthcare), and fluorescent signals were captured.

### Transmission electron microscopy (TEM)

The samples were diluted to an appropriate concentration with phosphate-buffered saline (PBS). The samples were fixed with 2% glutaraldehyde at room temperature. The fixed samples were applied to electron microscope grids and incubated at room temperature. Negative staining was performed by adding 10 µL of 2% phosphotungstic acid, after which the samples were completely dried in a dry environment. Finally, the particle morphology was observed.

### Preparation and characterization of transferrin (Tf)-modified liposomes (Tf-Lip-Ber)

Hydrogenated soybean phosphatidylcholine, transferrin-modified methoxy polyethylene glycol 2000 and cholesterol were mixed at a molar ratio of 8:1 and fully

dissolved in chloroform. Using a rotary evaporator at 40 °C, the chloroform was removed to form a dry, translucent lipid film, which was then hydrated with Ber solution at a molar ratio of 1:30 (Ber: lipid material). The hydrated liposome mixture was uniformly mixed by vortex oscillation and subsequently subjected to probe sonication (sonication parameters: 3 s on, 3 s off, 20% power, 30 min). To remove free Ber, ultrafiltration centrifugation was performed using a membrane with a specific molecular weight cutoff (MWCO: 3500 Da).

### Preparation and characterization of Tf-hEVs-Ber/Pal

Tf-Lip-Ber, Exo and Pal were vortexed at a particle number ratio of 1:2 and a drug molar ratio of 1:1. The mixture was incubated in a water bath at 37 °C for 1 h, resulting in the formation of Tf-hEVs-Ber/Pal. In this study, fluorescent dyes labeled Tf-hEVs-Ber/Pal were prepared by fusing dyes labeled Tf-Lip or Exos with drugs. Exo-Ber/Pal was prepared by fusing Exo, Ber and Pal. hEVs-Ber/Pal were prepared by fusing Exos, Lip-Ber and Pal.

The particle size distribution and zeta potential of Tf-hEVs-Ber/Pal were measured by DLS. The morphology of Tf-hEVs-Ber/Pal was observed via TEM. WB was performed to detect the expression of the exosomal markers TSG101, CD81, and CD26. To determine the encapsulation efficiency of Tf-hEVs-Ber/Pal, an appropriate amount of Tf-hEVs-Ber/Pal solution was transferred into the inner tube of an ultrafiltration centrifuge tube (MWCO: 3500 Da) and centrifuged at 4000 × g for 10 min. During this process, free drugs that were not encapsulated in vesicles passed through the ultrafiltration membrane into the outer tube, whereas the drugs encapsulated within the vesicles, owing to their larger particle size, remained in the inner tube. The filtrate from the outer tube was collected, and an appropriate sample was taken for the determination of Ber and Pal concentrations using HPLC to calculate the encapsulation efficiency.

Fluorescence resonance energy transfer (FRET) technology was used to assess the fusion of Tf-Lip-Ber with Exos, where FITC was used to label Tf-Lip-Ber (the donor) and DiI was used to label Exos (the acceptor). A suitable amount of purified Exos was incubated with DiI (final concentration of 5 µM) at 37 °C in the dark for 20 min. In parallel, FITC was added during the preparation of Tf-Lip-Ber using the film hydration method, ensuring that it dissolved together with the membrane material. The resulting preparations were then subjected to ultrafiltration centrifugation (MWCO: 3500 Da, 4000 × g, 10 min) to remove free dye, and resuspended in PBS. During FRET monitoring, the sample was irradiated with the excitation wavelength of FITC (488 nm). The buffer used was serum-free PBS to reduce background fluorescence interference. Negative controls were established

using DiI-Exos and FITC-Tf-Lip-Ber as single-label controls to eliminate cross-fluorescence interference.

To evaluate drug release, Tf-hEVs-Ber/Pal were placed in a dialysis bag with a molecular weight cutoff of 3500 Da. The dialysis bag was immersed in a beaker containing pH 7.4 PBS and gently stirred at 37 °C. Samples were collected at specific time points, and the released concentrations of Ber and Pal were quantified using HPLC (The operation methods and methodological supplements are included in Supplementary Material 2).

#### **Cellular uptake of Tf-hEVs-Ber/Pal and its uptake mechanism in vitro**

BV2 cells were seeded in culture dishes and coincubated with FITC-Tf-hEVs-Ber/Pal (FITC concentration of 125  $\mu\text{M}$ ) for various durations or with different concentrations of FITC-Tf-hEVs-Ber/Pal for 4 h. LysoTracker Red (50 nM) was added to the medium and incubated for 30 min to label the lysosomes. After incubation, the cells were washed with PBS to remove excess FITC-Tf-hEVs-Ber/Pal, fixed with paraformaldehyde (PFA) for 10 min, stained with DAPI for 10 min, and observed by confocal microscopy. Quantitative analysis was performed with flow cytometry (FCM). To investigate the route through which BV2 cells uptake FITC-Tf-hEVs-Ber/Pal, BV2 cells were incubated with colchicine (10  $\mu\text{M}$ ), nystatin (27  $\mu\text{M}$ ), beta-cyclodextrin (5 mM), or chlorpromazine (28  $\mu\text{M}$ ) for 30 min in advance.

#### **BBB penetration in vitro**

The in vitro BBB model was constructed with a transwell system. In brief, bEnd.3 cells were seeded in the upper chamber, and transendothelial cell resistance was measured *via* a trans-epithelial electrical resistance (TEER) meter. BV2 cells were seeded in the lower chamber when the TEER value exceeded 200  $\Omega\cdot\text{cm}^2$ . After overnight attachment, FITC-labeled Tf-hEVs-Ber/Pal (FITC concentration of 62.5  $\mu\text{M}$ ) were added to the upper chamber and incubated for 2 h. After incubation, the cells in the lower chamber were washed with PBS, fixed with 4% PFA for 10 min, stained with DAPI, and observed by confocal laser scanning microscopy (CLSM) and quantitative analysis by FCM.

To verify the TfR expression on bEnd.3 cells, a blank experiment was conducted, where cells were incubated with an anti-TfR (CD71) primary antibody overnight at 4 °C, washed with PBS, and then incubated with an Alexa Fluor 647-labeled secondary antibody at room temperature in the dark for 1 h. Further flow cytometry analysis was performed by incubating bEnd.3 cells with an anti-TfR (CD71) primary antibody for 30 min, followed by incubation with the Alexa Fluor 647-labeled secondary antibody at room temperature in the dark for 30 min. HEK293 cells were used as a negative control and treated

with the same antibodies. Additionally, a blank group was set up with no treatment. After all treatments, the cells were washed with PBS, resuspended in PBS, and analyzed by flow cytometry. To verify whether Tf-hEVs-Ber/Pal specifically bind to TfR on bEnd.3 cells, bEnd.3 cells were seeded into confocal dishes and divided into three groups: the experimental group was incubated with FITC-Tf-hEVs-Ber/Pal (62.5  $\mu\text{M}$ ) for 4 h; the competition group was pretreated with free Tf (100  $\mu\text{g}/\text{mL}$ , 30 min) to block TfR, followed by incubation with FITC-Tf-hEVs-Ber/Pal (62.5  $\mu\text{M}$ ) for 4 h. After incubation, all groups of cells were washed with PBS, fixed with 4% paraformaldehyde. The nuclei were stained with DAPI for 10 min. Confocal microscopy was used to detect FITC-Tf-hEVs-Ber/Pal (green, 488 nm), TfR (CD71) (red, 647 nm), and DAPI (blue, 405 nm) signals. Flow cytometry was used to analyze the uptake of Tf-hEVs-Ber/Pal in bEnd.3 cells. The bEnd.3 cells were divided into the experimental group and the competition group. The experimental group was incubated with FITC-Tf-hEVs-Ber/Pal (62.5  $\mu\text{M}$ ) for 4 h, while the competition group was pretreated with free Tf (100  $\mu\text{g}/\text{mL}$ , 30 min) and then incubated with FITC-Tf-hEVs-Ber/Pal (62.5  $\mu\text{M}$ ) for 4 h. As a negative control, HEK293 cells were treated using the same method as the bEnd.3 cells. After all treatments, the cells were washed with PBS and resuspended in PBS for flow cytometry analysis.

#### **Anti-inflammatory effects of Tf-hEVs-Ber/Pal in vitro**

BV2 cells were seeded in culture dishes and cultured until the cell density reached 80%. BV2 cells were incubated with LPS (166  $\mu\text{M}$ ) for 24 h to induce an inflammatory response and establish an inflammation model. Then, Tf-hEVs, Ber, Pal, the Ber/Pal physical mixture, hEVs-Ber/Pal, Tf-hEVs-Ber, Tf-hEVs-Pal, and Tf-hEVs-Ber/Pal were added. The final concentration of Ber and Pal was 1  $\mu\text{M}$ . The blank group was treated with medium replacement only. After incubation for 24 h, the supernatant medium was collected, and the NO content was measured using a Griess reagent kit. The IL-1 $\beta$ , IL-4, IL-10, and TNF- $\alpha$  levels in the supernatant were quantified using enzyme-linked immunosorbent assay (ELISA) kits.

#### **In vivo distribution of Tf-hEVs-Ber/Pal**

C57BL/6J mice (6–8 weeks) were acclimatized to the testing environment for one week. The DiI-free dye DiI-hEVs-Ber/Pal or DiI-Tf-hEVs-Ber/Pal was administered by tail vein injection at a DiI dose of 5 mg/kg. Small animal in vivo imaging was performed at specific time points using an IVIS (excitation wavelength of 748 nm and emission wavelength of 780 nm). The mice were anesthetized using a gas anesthesia machine, with the oxygen flow rate set to 1 L/min and the isoflurane concentration set to 3%. After anesthesia, the mice were placed in the scanning

area of the imaging device for whole-body imaging to obtain fluorescence images of the drug distribution in the body. After imaging, the mice were euthanized, and their major organs (heart, liver, kidney, lung, spleen, and brain) were collected and scanned to analyze the distribution and accumulation of the drug in each organ.

#### AD mouse model construction

The AD mouse model used in the study was described previously [29, 30]. C57BL/6J mice (6–8 weeks) were acclimatized for one week before the experiment. The mice were anesthetized with isoflurane (4%) using a gas anesthesia machine. After anesthesia, the mice were placed in a stereotaxic apparatus, and the fur on their heads was trimmed using surgical scissors. A small incision was made on the scalp to expose the skull surface, and the hippocampal region was located at the following coordinates: anterior-posterior (AP) -2.0 mm, medial-lateral (ML) +1.5 mm, and dorsal-ventral (DV) 1.5 mm. Using a microsyringe, 5  $\mu$ L of A $\beta$  protein solution (5  $\mu$ g/ $\mu$ L) was slowly injected into the hippocampal region at a rate of 1  $\mu$ L/min. After injection, the needle was held in place for 30 s before being withdrawn slowly. The scalp was sutured using fine thread, and iodine tincture was applied for disinfection. The mice were then placed in a warm area until they fully recovered from anesthesia. The recovery period lasted for one week after the surgery.

#### Administration and behavioral detection

The control group was not subjected to any treatment. After the recovery period, different formulations (Saline, Tf-hEVs, Ber, Pal, Ber/Pal physical mixture, hEVs-Ber/Pal, Tf-hEVs-Ber, Tf-hEVs-Pal, and Tf-hEVs-Ber/Pal) were administered through the tail vein every two days. Ber (1.27 mg/kg) and Pal (1.60 mg/kg) were administered to each mouse.

#### Morris water maze (MWM) test

Water maze training began after five treatment sessions. From Days 1 to 5, water maze training was conducted with the pool water level maintained 1–2 cm above the platform and the water temperature maintained at 25 °C. Visual cues of different shapes and colors were placed in the four quadrants of the pool, with the platform located in the target quadrant. The mice were placed in different quadrants of the pool for training. Each training session lasted for 60 s. If the mouse failed to locate the platform within 60 s, it was guided to the platform and allowed to stay there for 10 s. The latency to find the platform, the time spent in the target quadrant, the movement path, and the number of platform crossings were recorded to assess spatial learning ability. On Day 6, a probe test was conducted in the water maze, with the platform removed. The mice were placed in the farthest quadrant from the

target quadrant and allowed to swim freely for 60 s. The time spent in the target quadrant and the swimming path were recorded to evaluate spatial memory and cognitive function.

#### Novel object recognition (NOR) test

The novel object recognition test involves an adaptation phase, training phase and test phase. First, the mice were placed in an empty experimental box for 10 min per day for two consecutive days to reduce their stress to the environment. Two identical objects were subsequently placed in the box, and the mice were allowed to explore for 5 min. After the exploration period ended, the test box and objects were cleaned with 75% alcohol to remove any residual odors. For the test phase, one of the objects was replaced with a new one, and the mice were allowed to explore freely for another 5 min. The time spent exploring the new object and the old object was recorded. The following formula is used to calculate the recognition index (RI) for the novel object.  $RI = \frac{T_{novel}}{T_{familiar} + T_{novel}}$

$T_{novel}$  is the time the animal spends in front of the novel object, and  $T_{familiar}$  is the time the animal spends in front of the familiar object.

#### Experimental sampling

The mice were anesthetized using a gas anesthesia machine. An incision was made along the midline of the chest with surgical scissors, and the heart, liver, spleen, lungs, and kidneys were removed. The organs were rinsed with physiological saline, placed in cryovials, and then stored at -80 °C. The skull was opened, and the entire brain was carefully extracted. The extracted brain tissue was placed in physiological saline.

#### Immunofluorescence observation

The collected brains were divided to isolate the hippocampus, prefrontal cortex, and striatum and placed in 4% PFA solution overnight for fixation. The fixed brain tissue was dehydrated with a gradient alcohol series and then immersed in paraffin. The tissue was cut into 5  $\mu$ m-thick sections using a microtome. The sections were deparaffinized by immersion in xylene for complete removal of paraffin and then washed with a series of graded ethanol solutions (100%, 95%, 80%, and 70%) for rehydration. Antigen retrieval was performed by immersing the sections in citrate buffer (pH 6.0) and heating them in a microwave or water bath for 10–15 min to unmask the antigens. After antigen retrieval, the sections were allowed to cool naturally to room temperature, then thoroughly washed three times with PBS to remove any residual buffer and prepare the sections for further staining procedures. Then, the sections were blocked with 5% BSA solution at room temperature for 30 min. The

diluted TH-S, neuronal nuclei (NeuN), and primary antibodies for M1 and M2 polarization of microglia were added to the sections, which were then incubated overnight at 4 °C, followed by three washes with PBS buffer for 10 min per wash. The sections were incubated with Alexa Fluor 488-labeled, Cy3-labeled, phycoerythrin (PE)-labeled, and FITC-labeled secondary antibodies at room temperature for 1 h and washed again with PBS three times for 10 min each. Subsequently, DAPI was added for 10 min to stain the nuclei. Observation was conducted using a fluorescence microscope with appropriate excitation wavelengths and filters. The mean TH-S fluorescence intensity, the number of NeuN-positive neurons, and the average fluorescence intensity of M1 and M2 were quantitatively analyzed via ImageJ software.

To investigate the expression of NF- $\kappa$ B p65 and p38 MAPK in the hippocampal tissue of different treatment groups, we performed WB analysis. Total protein was extracted from the hippocampal tissue of the mice in each group, and the protein concentration was measured. SDS-PAGE electrophoresis was then performed, followed by membrane transfer. The detailed experimental procedure is described in Sect. 2.2. The membranes were incubated with primary antibodies (anti-NF- $\kappa$ B p65, anti-p38 MAPK) overnight, washed with TBST for 3 times (10 min per time), then, incubated with the secondary antibodies for 4 h. The protein bands were scanned with the gel imaging system. After development, the band intensities were analyzed using ImageJ software, and the relative expression of target proteins was calculated using GAPDH as the internal reference.

#### Safety evaluation of Tf-hEVs-Ber/Pal

The serum samples from each group were thawed at room temperature and processed according to the instructions of the corresponding kits. ALT, AST, CREA, BUN, ALB, and TP levels were measured using biochemical assay kits following the kit instructions, and the data were obtained with a microplate reader. Whole blood samples from each group were placed into test tubes for analysis using a hematology analyzer, and the sample was automatically loaded into the analyzer to measure routine parameters, including white blood cell (WBC) count, red blood cell (RBC) count, hemoglobin (Hb) concentration, and platelet (PLT) count.

#### Statistical analysis

The data in the figure are expressed as the means  $\pm$  standard deviations. Statistical analysis was performed using Student's *t* test: \* $P < 0.05$ , \*\* $P < 0.01$ , \*\*\* $P < 0.001$ , # $P < 0.05$ , ## $P < 0.01$ , ### $P < 0.001$ , ns indicates not statistically significant. \* Indicates a significant difference between the control group and the model group, as well as between the chlorpyrifos treatment group and the PBS treatment

group. Additionally, comparisons of DiR-Tf-hEVs-Ber/Pal vs. DiR, DiR-hEVs-Ber/Pal, FITC-Tf-hEVs-Ber/Pal vs. FITC, FITC-Exo-Ber/Pal, FITC-hEVs-Ber/Pal, and FITC-Tf-Lip-Ber/Pal were performed. # indicates a significant difference between the Tf-hEVs-Ber/Pal group and the other treatment groups.

## Results

### Preparation and characterization of Tf-hEVs-Ber/Pal

As shown in Fig. 1A, Tf-hEVs-Ber/Pal were prepared in a two-step process. First, Ber-loaded liposomes (Tf-Lip-Ber) were prepared by the film dispersion method. Subsequently, Tf-Lip-Ber, Exo and Pal were mixed in certain proportions, and Tf-hEVs-Ber/Pal hybrid nanovesicles were prepared via the water-bath method. The optimal manufacturing parameters for Tf-Lip-Ber resulted in a high Ber loading capacity (2.53%) and encapsulation efficiency (77.45%) (Table S1). These preparation parameters were a membrane material ratio of 8:1, a drug-to-lipid ratio of 1:30, an ultrasonication duration of 30 min, and an ultrasound power of 20%. The particle size analysis and shape characterization revealed that the average size of Tf-Lip-Ber was approximately 150 nm (Fig. S1A), with typical spherical nanoparticle characteristics (Fig. S1B), and that the particle size remained stable for 48 h (Fig. S1C). The Exos purified from the supernatant of BV2 cell culture using size-exclusion chromatography had a particle size of approximately 110 nm (Fig. S1D) and typical teacup-shaped or round structures (Fig. S1E) [31, 32]. CD81, TSG101, and Alix have been reported as reliable membrane markers of exosomes [33]. These specific proteins were analyzed by WB, further confirming the successful isolation and purification of Exos (Fig. S1F).

Lips and Exos have similar vesicle structures and are prone to membrane fusion, and common methods include the water incubation method and the repeated freeze-thaw method [34, 35]. In summary, both methods could be used to prepare Tf-hEVs-Ber/Pal successfully, and no significant differences were observed in terms of particle size, zeta potential or specific membrane proteins (Fig. 1B-D). After fusion with Tf-Lip-Ber, exosome protein expression was retained, preserving exosomal characteristics such as homing targeting (Fig. 1D) [36]. However, DLS measurements revealed changes in the polydispersity index (PDI), and the water bath method yielded more stable Tf-hEVs-Ber/Pal (PDI < 0.3) without significant aggregation or dispersion of particles (Fig. 1E). The water bath method enables a more uniform and gentle fusion process of exosomes and liposomes, avoiding severe disturbances to the membrane structure, whereas dramatic temperature changes during repeated freeze-thaw cycles may result in the uneven rearrangement of phospholipid molecules [37–40]. Hence, the water bath

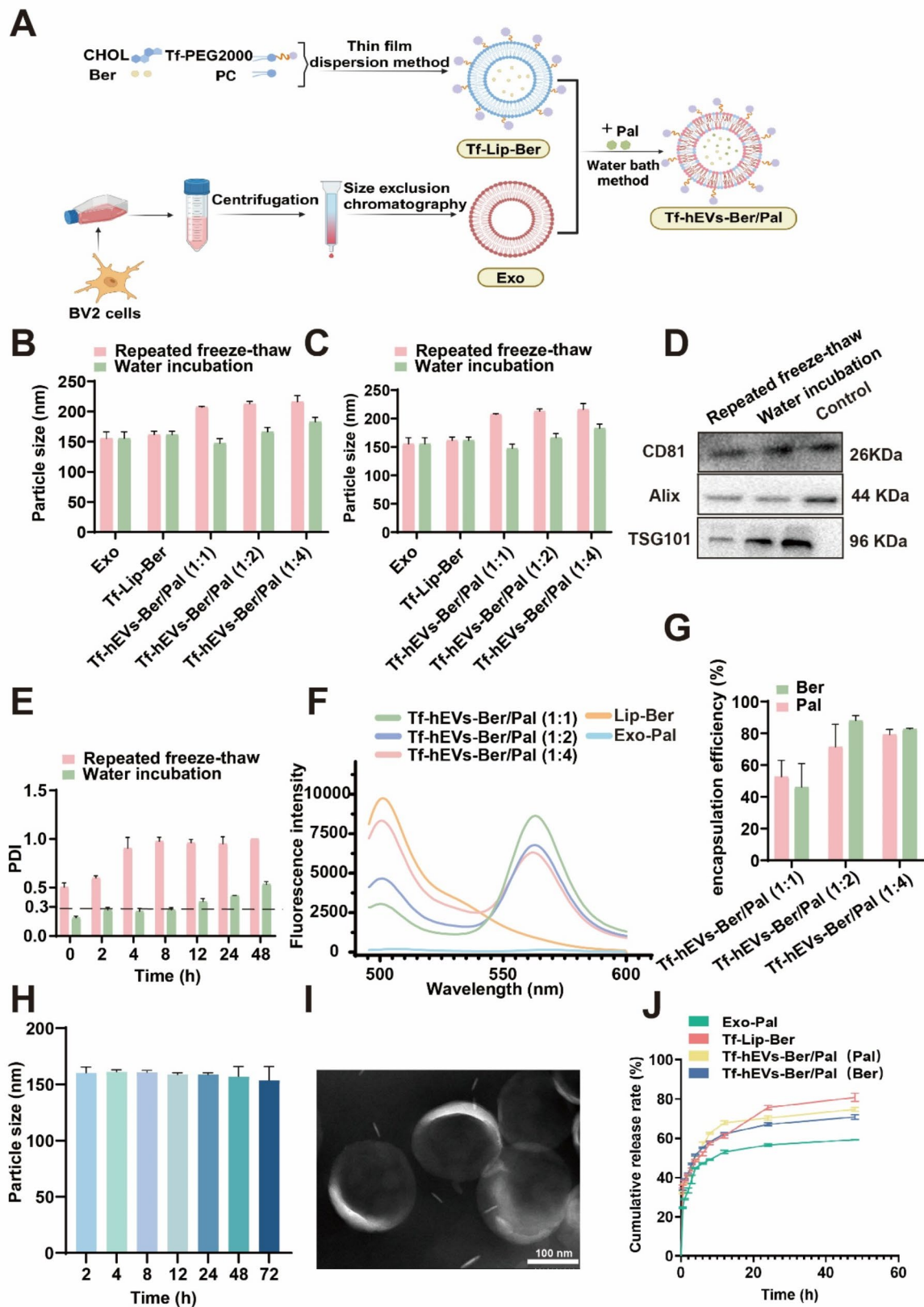


**Fig. 1** (See legend on next page.)

(See figure on previous page.)

**Fig. 1** Investigation and characterization of Tf-hEVs-Ber/Pal. **(A)** Tf-hEVs-Ber/Pal were prepared via a two-step process. **(B)** The particle size and **(C)** zeta potential of the particles and **(D)** protein expression of CD81, Alix and TSG101 in Tf-hEVs-Ber/Pal were analyzed by WB. Control represents the purified Exos. **(E)** Changes in the PDI of Tf-hEVs-Ber/Pal obtained by repeated freeze–thaw cycles and incubation methods within 48 h were measured with a Malvin particle size meter. **(F)** FRET spectrum of DiL and FITC-stained Tf-hEVs-Ber/Pal was determined by a fluorescence spectrophotometer. Before fusion, Exos were stained with DiL, and Tf-Lips were stained with FITC. **(G)** Encapsulation efficiency of Tf-hEVs-Ber/Pal obtained by different fusion methods with different particle ratios of Exo and Tf-Lip-Ber. **(H)** Stability of Tf-hEVs-Ber/Pal. The change in the particle size of Tf-hEVs-Ber/Pal after 3 days was measured by DLS. **(I)** TEM image of Tf-hEVs-Ber/Pal. Scale bar, 100 nm. **(J)** Cumulative drug release profiles of Ber and Pal from Tf-hEVs-Ber/Pal, Tf-Lip-Ber, and Exo-Pal were determined using the dialysis method in PBS (pH 7.4) to simulate cerebrospinal fluid over 48 h. Data are presented as the means  $\pm$  SDs ( $n=3$ )

method was selected for the preparation of Tf-hEVs-Ber/Pal.

The FRET technique is very practical for investigating the interactions between two elements in hybrid systems [41, 42]. The FRET donor and acceptor dyes were loaded into the liposomes and exosomes, respectively. The FRET phenomenon, which occurs due to the close proximity of the donor and acceptor dyes, will be observed only if the hybrid vehicle is successfully formed. Two dyes labeled Tf-hEVs-Ber/Pal were prepared by fusing FITC-labeled Tf-Lips (donor, 488 nm/525 nm for ex/em) and DiL-labeled exosomes (acceptor, 551 nm/569 nm for ex/em). As shown in Fig. 1F, obvious FRET signals were observed in Tf-hEVs-Ber/Pal, in which energy was transferred from the donor to the receptor, confirming successful fusion of Exos and Tf-Lips at various particle ratios. Additionally, the encapsulation efficiency of Ber and Pal was greater when the fusion particle ratio of Exo to Tf-Lip was 1:2 than when the other particles ratios were used, with values of approximately 70% and 90% for Ber and Pal, respectively (Fig. 1G). Therefore, the particle ratio of Exos to Tf-Lip in the Tf-hEVs-Ber/Pal formulation was set to 1:2 to minimize the amount of Exos used. The particle size of Tf-hEVs-Ber/Pal did not vary significantly over 72 h (Fig. 1H), indicating good physicochemical stability under physiological conditions. Moreover, the particle size of Tf-hEVs-Ber/Pal was 166.2 nm, with a zeta potential of  $-4.79$  mV, and it was well dispersed in the solution. TEM observation of Tf-hEVs-Ber/Pal revealed spherical vesicles with diameters of approximately 150–180 nm (Fig. 1I).

Drug release from Tf-hEVs-Ber/Pal, Tf-Lip-Ber, and Exo-Pal in pH 7.4 fluid was assessed via dialysis over 48 h (Fig. 1J). The experimental results indicated that different carrier systems significantly influenced the release kinetics of Ber and Pal. The Tf-Lip-Ber group exhibited the fastest release rate of Ber, with a cumulative release of 80.88% over 48 h. In contrast, the Exo-Pal group showed the slowest Pal release, only 59.30%. The release rate of the Tf-hEVs-Ber/Pal group was intermediate, with Pal and Ber release rates of 70.87% and 74.76% at 48 h, respectively. In addition, Ber and Pal are released from Tf-hEVs-Ber/Pal almost simultaneously. These findings indicate that Tf-hEVs-Ber/Pal provide stable drug release, ensuring sustained and balanced therapeutic effects, reducing drug concentration fluctuations, and

prolonging the effects of Ber and Pal on microglia [36, 43, 44].

#### Cellular uptake of Tf-hEVs-Ber/Pal

FITC-labeled Tf-hEVs-Ber/Pal were incubated with BV2 microglia to analyze their cellular uptake at different incubation times and drug concentrations (Fig. 2A–D). CLSM imaging and flow cytometry revealed that the uptake of Tf-hEVs-Ber/Pal by BV2 cells increased over time, indicating a time-dependent process (Fig. 2A–B and Fig S2A). Additionally, cellular uptake accelerated with increasing concentrations of FITC-Tf-hEVs-Ber/Pal, suggesting a concentration-dependent uptake mechanism (Fig. 2C–D and Fig S2B). The endocytic pathways of Tf-hEVs-Ber/Pal in BV2 cells were studied by pretreating the cells with various inhibitors. The results revealed that the cellular uptake of FITC-Tf-hEVs-Ber/Pal was significantly inhibited with chlorpromazine treatment (Fig. 2E). The cellular uptake of FITC-Tf-hEVs-Ber/Pal in BV2 cells decreased by approximately 90% in response to chlorpromazine (Fig. 2F and Fig S2C). Chlorpromazine blocks clathrin-mediated endocytosis [45, 46], indicating that Tf-hEVs-Ber/Pal primarily enter cells via clathrin-mediated endocytosis and has lysosomal escape potential. Furthermore, CLSM was used to examine the intracellular distribution of Tf-hEVs-Ber/Pal and its colocalization with lysosomes. The results revealed that FITC-Tf-hEVs-Ber/Pal (green fluorescence) showed minimal colocalization (yellow fluorescence) with the lysosomal marker (red fluorescence), suggesting that Tf-hEVs-Ber/Pal can evade lysosomal degradation and is not captured by lysosomes (Fig. 2G). Overall, Tf-hEVs-Ber/Pal can enter BV2 cells through clathrin-mediated endocytosis and successfully evade lysosomal degradation, which is essential for its anti-inflammatory effects, as proinflammatory targets are always distributed in the cytoplasm [47].

#### Anti-inflammatory effects of Tf-hEVs-Ber/Pal in vitro

The uptake of Tf-hEVs-Ber/Pal was necessary for it to exert its therapeutic effects. To verify whether Tf-hEVs-Ber/Pal can inhibit AD-related inflammatory responses after being internalized by BV2 microglia, an LPS-stimulated inflammatory model was established in BV2 cells. LPS treatment significantly increased the release of NO, IL-1 $\beta$ , and TNF- $\alpha$ , successfully mimicking the robust inflammatory responses of microglia observed in the

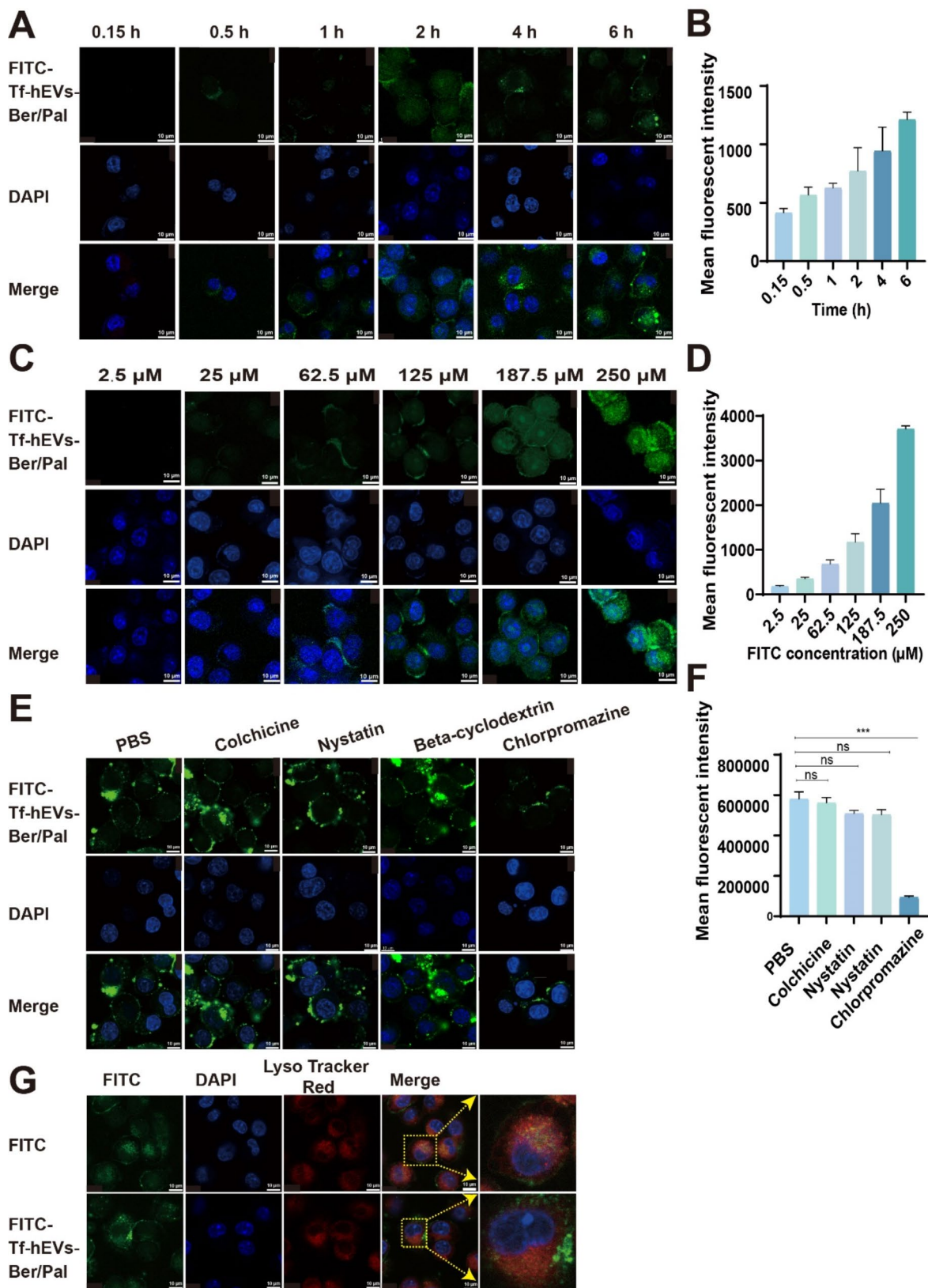


**Fig. 2** (See legend on next page.)

(See figure on previous page.)

**Fig. 2** Cellular uptake of Tf-hEVs-Ber/Pal in vitro. The cellular uptake of FITC (green)-labeled Tf-hEVs-Ber/Pal with increasing (A) time and (C) concentration was determined by CLSM. (B and D) The quantitative determination of cellular uptake was performed via flow cytometry. The concentration of FITC was 125  $\mu\text{M}$ , and the incubation time was 4 h. (E) CLSM observation and (F) quantitative analysis of intracellular accumulation. BV2 cells were preincubated with different endocytic pathway blockers for 30 min and then incubated with FITC-stained Tf-hEVs-Ber/Pal for 2 h. The concentration of FITC was 250  $\mu\text{M}$ . (G) Lysosomal escape of FITC-labeled Tf-hEVs-Ber/Pal was observed by CLSM. BV2 cells were incubated with FITC-Tf-hEVs-Ber/Pal for 4 h and then incubated with LysoTracker Red for 30 min. The colocalization of Tf-hEVs with lysosomes is displayed in yellow. The nuclei of BV2 cells were stained with DAPI (blue). Scale bar, 10  $\mu\text{m}$ . The data are presented as the means  $\pm$  SDs ( $n=3$ )

pathological process of AD (Fig. 3) [48–51]. Compared with the other formulations, the Tf-hEVs-Ber/Pal formulation significantly reduced the release of proinflammatory factors (NO, IL-1 $\beta$ , and TNF- $\alpha$ ; Fig. 3A-C) and notably increased the levels of anti-inflammatory factors (IL-4 and IL-10; Fig. 3D-E), indicating the optimal inflammation balance ability. Specifically, compared with the Ber/Pal physical mixture treatment, the Tf-hEVs-Ber/Pal treatment reduced NO levels by 43.61%, IL-1 $\beta$  by 25.05%, and TNF- $\alpha$  by 43.61%, while increasing IL-4 and

IL-10 levels by 34.03% and 30.78%, respectively, further demonstrating that the hybrid vesicle (Tf-hEVs) coating was beneficial for the suppression of AD-related inflammation by Ber/Pal. By specifically delivering the anti-inflammatory agents Ber and Pal, Tf-hEVs-Ber/Pal not only effectively inhibited proinflammatory responses but also significantly increased the secretion of anti-inflammatory factors, potentially preventing or mitigating the progression of microglia-related AD neuroinflammation.

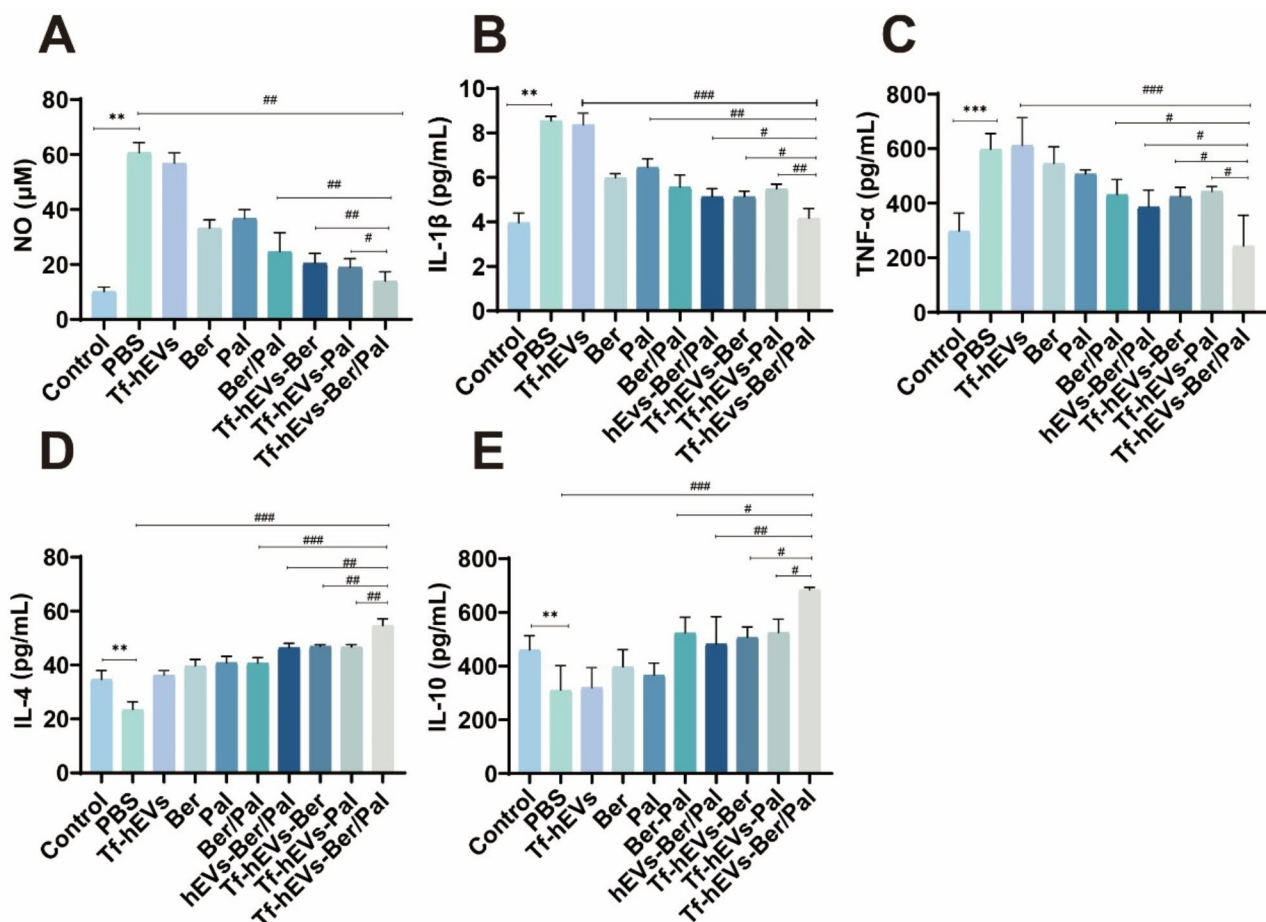


**Fig. 3** The anti-inflammatory effects of Tf-hEVs-Ber/Pal in vitro. (A) The NO concentration was determined via the Griess reagent method. (B-E) The concentrations of microglial proinflammatory cytokines (IL-1 $\beta$  and TNF- $\alpha$ ) and anti-inflammatory cytokines (IL-4 and IL-10) were measured via enzyme-linked immunosorbent assay. LPS (166  $\mu\text{M}$ ) was used to stimulate BV2 cells for 24 h to establish an inflammatory model, and a control group of normal BV2 cells was established. Tf-hEVs, Ber, Pal, the Ber/Pal physical mixture, hEVs-Ber/Pal, Tf-hEVs-Ber, Tf-hEVs-Pal, and Tf-hEVs-Ber/Pal were incubated with activated BV2 cells for 24 h. The final concentration of Ber and Pal was 1  $\mu\text{M}$ . The data are presented as the means  $\pm$  SDs ( $n=6$ ). Statistical analysis was performed using Student's *t* test: \* $P < 0.05$ , \*\* $P < 0.01$ , \*\*\* $P < 0.001$ . # $P < 0.05$ , ## $P < 0.01$ , ### $P < 0.001$

### Increased transport of Tf-hEVs-Ber/Pal across the BBB in vitro

In this study, Tf modification of hybrid vesicles may enable Tf-hEVs-Ber/Pal to traverse the BBB via receptor-mediated transcytosis, facilitating the transport of Ber and Pal across the BBB for AD therapy [52]. To further verify the specific binding of Tf-hEVs-Ber/Pal with TfRs and explore the rationality of the model cells (bEnd.3 cells), we conducted confocal microscopy and flow analysis. As shown in the Fig. S3A, we used DAPI (blue) to stain the cell nuclei and an anti-CD71 antibody (red) to label the TfR, confirming the expression of TfR on the surface of bEnd.3 cells. Furthermore, the flow cytometry was performed (Fig. S3B) to quantitatively evaluate the TfR expression on the cell surface (Fig. S3C). It has been reported that HEK293 cells exhibit minimal expression of the TfR and are suitable for use as a negative control [53, 54]. As result, the strong fluorescence intensity indicated the bEnd.3 cells significantly ( $P < 0.001$ ) expressed TfR, while HEK293 cells showed minimal fluorescence under the same conditions, demonstrating the bEnd.3 cells were helpful for the in vitro BBB model construction [55]. To further validate the specific binding of Tf-hEVs-Ber/Pal with TfR (Fig. S3D), high concentration of free Tf was used as the competition drugs of Tf-hEVs-Ber/Pal. In the competition group, bEnd.3 cells were pretreated with high concentrations of free Tf, followed by incubation with FITC-labeled Tf-hEVs-Ber/Pal, while bEnd.3 cells were directly incubated with FITC-labeled Tf-hEVs-Ber/Pal in the normal group. The results revealed that the fluorescence signal of FITC-labeled Tf-hEVs-Ber/Pal in the competition group was significantly weakened, indicating that free Tf inhibited the binding of Tf-hEVs-Ber/Pal with TfR. Flow cytometry analysis was further conducted (Fig. S3E), along with quantitative evaluation (Fig. S3F). The cellular uptake of Tf-hEVs-Ber/Pal in the bEnd.3 cells was significantly inhibited in the Tf competition group ( $P < 0.001$ ), which was consistent with the confocal observation. In addition, there are no differences were discovered in the HEK293 cells. These findings confirmed that the binding of Tf-hEVs-Ber/Pal with TfR is specific and dependent on TfR, which demonstrated the Tf-hEVs-Ber/Pal have superior ability to penetrate the BBB.

The widely reported in vitro Transwell model comprising bEnd.3 cells and BV2 cells was constructed as illustrated in Fig. 4A [56, 57]. The upper chamber seeded with bEnd.3 cells was incubated with FITC, FITC-Exo-Ber/Pal, FITC-hEVs-Ber/Pal, FITC-Tf-Lip-Ber/Pal, or FITC-Tf-hEVs-Ber/Pal. The cellular uptake of these formulations by BV2 microglia in the lower chamber was then observed *via* CLSM and quantified using flow cytometry (Fig. 4B-D). The results revealed that Tf decoration progressively increased drug endocytosis in BV2 cells after BBB transcytosis. The Tf-Lip-Ber/Pal and Tf-hEVs-Ber/

Pal groups presented stronger and brighter green fluorescence (Fig. 4B). Compared with FITC, FITC-Exo-Ber/Pal, and FITC-hEVs-Ber/Pal, Tf-Lip-Ber/Pal and Tf-hEVs-Ber/Pal exhibited approximately double and triple the fluorescence intensity, respectively (Fig. 4D). This highlights the advantages of the interaction between Tf and the transferrin receptor (TfR) [52]. Compared with Tf-Lip-Ber/Pal, Tf-hEVs-Ber/Pal further increased cellular endocytosis in lower BV2 cells ( $P < 0.05$ ), which may have contributed to the high affinity and “homing effect” of Tf-hEVs-Ber/Pal (containing BV2-derived Exos) on BV2 cells [58]. These findings demonstrated that Tf-hEVs-Ber/Pal were effective nanocarriers capable of efficiently delivering therapeutic agents across the BBB and achieving superior microglia-targeting performance, which could improve the efficacy of anti-inflammatory agents (Ber and Pal herein) and AD therapy via microglia-targeted delivery [48]. These findings further confirmed that Tf-hEVs-Ber/Pal could effectively penetrate the cell membrane through the TfR-mediated pathway, enhancing its ability to cross the BBB.

### Brain targeting ability of Tf-hEVs-Ber/Pal in vivo

Owing to the complicated and unpredictable differences between cellular and organismal systems [59, 60], the brain targeting ability of Tf-hEVs-Ber/Pal was further investigated in C57BL/6J mice. After injecting DiR-labeled preparations into C57BL/6J mice, we monitored the biodistribution and accumulation of DiR-Tf-hEVs-Ber/Pal in the brain using an in vivo imaging system (IVIS) (Fig. 5). The results revealed that the fluorescence intensities of the free drug and hEVs-Ber/Pal groups in the brain were significantly inferior to that of the Tf-hEVs-Ber/Pal group, which is consistent with the in vitro results. Moreover, the Tf-hEVs-Ber/Pal group rapidly circulated to the brain within 2 h postinjection and peaked by 8 h, with Tf-hEVs-Ber/Pal accumulation occurring over 24 h (Fig. 5A and C). The mice were subsequently euthanized, and major organs were harvested at different time points postinjection for ex vivo imaging (Fig. 5B). The hybrid vesicles of DiR-Tf-hEVs-Ber/Pal accumulated more in the brain than DiR and DiR-hEVs-Ber/Pal did, approximately 2.06 times and 1.30 times greater, respectively, at 8 h (Fig. 5D,  $P < 0.05$ ). Tf-hEVs-Ber/Pal has superior targeting properties. According to our mechanistic analysis, Tf-hEVs-Ber/Pal can specifically bind to TfRs in the cerebral vasculature. Moreover, under pathological AD-like conditions, the expression of TfR is significantly upregulated in brain endothelial cells, which may further increase the targeting ability of Tf-modified formulations, allowing them to rapidly accumulate at diseased sites [61, 62]. These findings indicate that Tf-hEVs-Ber/Pal could deliver Ber/Pal into the brain, which could increase the efficacy of the formulation in treating AD.

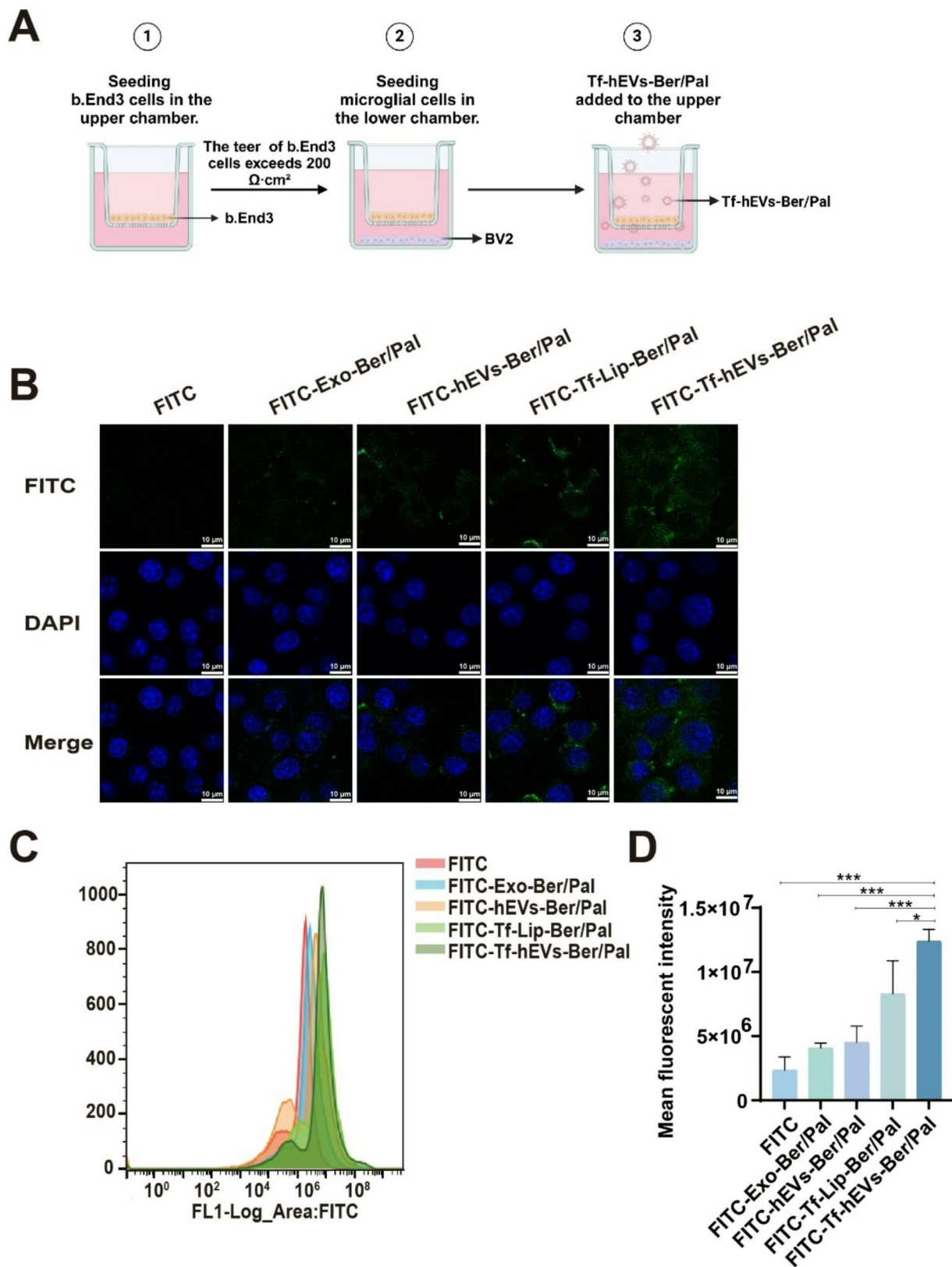


**Fig. 4** (See legend on next page.)

(See figure on previous page.)

**Fig. 4** The transport of Tf-hEVs-Ber/Pal across the BBB in vitro. **(A)** Schematic illustration of the in vitro BBB model. bEnd.3 cells and BV2 cells were seeded in the upper and lower chambers, respectively. FITC-stained Tf-hEVs-Ber/Pal were added to the upper chamber when the transmembrane electrical resistance of the cells exceeded  $200 \Omega \cdot \text{cm}^2$ . BV2 cells in the lower chamber were collected after the addition of different formulations for 2 h and analyzed by **(B)** CLSM and **(C and D)** flow cytometry. The concentration of FITC was  $62.5 \mu\text{M}$ . FITC (green), DAPI (blue). Scale bar,  $10 \mu\text{m}$ . The data are presented as the means  $\pm$  SDs ( $n=3$ ). \* $P < 0.05$ , \*\* $P < 0.01$ , \*\*\* $P < 0.001$

### Tf-hEVs-Ber/Pal improved the behavioral and cognitive performance of AD model mice

In this study, an AD mouse model was established via the injection of A $\beta$  protein into the hippocampi of C57BL/6J mice through surgery after they were allowed to adapt to the testing environment for one week; this AD model has been widely reported in previous articles [63–65]. The entire experimental process is illustrated in Fig. 6A. The MWM and NOR tests were conducted to test the behavior of AD model mice after the administration of different formulations. In the MWM test, the mice were trained for five days, followed by an escape experiment on day six to evaluate their spatial learning and memory capabilities. The better their spatial memory is, the shorter the time taken to find the platform, the higher the frequency of crossing the target platform, and the longer the time spent lingering in the target quadrant. The representative swimming trajectories of the different groups on day six are shown in Fig. 6B. The escape latency during the training period was recorded, as shown in Fig. 6C. Mice treated with Tf-hEVs-Ber/Pal spent the least amount of time finding the platform, and the latency clearly decreased. As shown in Fig. 6D, the mice in the blank group crossed the platform approximately 5–7 times, whereas the mice in the saline groups crossed the platform only 0–2 times, indicating that the memory function of the AD model mice was severely impaired. Posttreatment with Ber or Pal, Ber/Pal, hEVs-Ber/Pal, a single drug loaded with Tf-hEVs or Tf-hEVs-Ber/Pal increased the number of platform crossings to various degrees. Compared with the other groups, the Tf-hEV-Ber/Pal therapy group exhibited significant improvement, with an increase of 3–6-fold. The time and distance traveled in the target quadrant further demonstrated spatial learning ability (Fig. 6E and F) [66, 67]. The mice in the blank group spent 60% of the total time in the target quadrant, whereas the mice in the saline group spent only 17%. In contrast, the percentage of time spent in the target quadrant significantly increased in the Tf-hEVs-Ber/Pal-treated groups, reaching nearly 60%, indicating a more focused swimming trajectory in the target quadrant (Fig. 6E). Compared with the saline group, the Tf-hEVs-Ber/Pal group presented the greatest distance traveled in the target quadrant, with a 207.05% increase (Fig. 6F). To further validate the above results, we conducted a novel object recognition (NOR) test (Fig. 6G). The RI was calculated to assess the ability of the mice to recognize the novel object, thereby reflecting their learning and

memory abilities. The RI in the saline group was significantly reduced to approximately 43.17%, indicating that AD impaired the ability of the mice to recognize the novel object effectively and impaired their learning and memory abilities. The Tf-hEVs-Ber/Pal group presented the greatest percentage of time spent investigating the novel object, approximately 77.52%, which was approximately 1.8 times greater than that of the saline group and significantly greater than that of the other treatment groups, approaching the level of the control group. These results indicate that the Tf-hEVs-Ber/Pal had predominant effects on enhancing spatial cognitive ability, restoring memory and improving cognitive function in AD model mice.

Studies have reported that Ber reduces neuronal damage by inhibiting A $\beta$  aggregation and tau protein phosphorylation and that Pal has the potential to modulate neuroinflammation and promote neuronal regeneration. The combination of Ber and Pal may act on multiple key pathological pathways of AD, thereby enhancing therapeutic efficacy [68–75]. The Tf-hEVs-Ber/Pal system combines the advantages of transferrin modification with the natural targeting capability of exosomes, enabling Ber and Pal to efficiently penetrate the BBB. This increases their bioavailability, significantly enhances their therapeutic effects, and notably improves the spatial memory and learning behaviors of AD model mice.

### Tf-hEVs-Ber/Pal relieved A $\beta$ accumulation and neuroinflammation in AD model mice

Reducing A $\beta$  deposition is essential for improving cognitive function and alleviating AD pathology [76, 77]. We used immunofluorescence staining to observe A $\beta$  sedimentation in the hippocampus to assess the effects of Tf-hEVs-Ber/Pal therapy on AD mice (Fig. 7A). Compared with those in the other treatment groups, the fluorescence intensity in the hippocampus in the Tf-hEVs-Ber/Pal treatment group was significantly lower. Semiquantitative analysis revealed that Tf-hEVs-Ber/Pal decreased the number of A $\beta$  plaques individually (in contrast to saline), 3–4.5-fold (in contrast to free drugs), and 2-fold (compared with single drug loading) (Fig. 7B). These findings suggested that Tf-hEVs-Ber/Pal could effectively intervene in A $\beta$  metabolism and accelerate A $\beta$  clearance. Furthermore, we measured A $\beta$ -40 and A $\beta$ -42 levels via ELISA. The results showed that Tf-hEVs-Ber/Pal treatment significantly decreased the expression levels of A $\beta$ -40 and A $\beta$ -42 in the brain (Fig. 7C and D), demonstrating

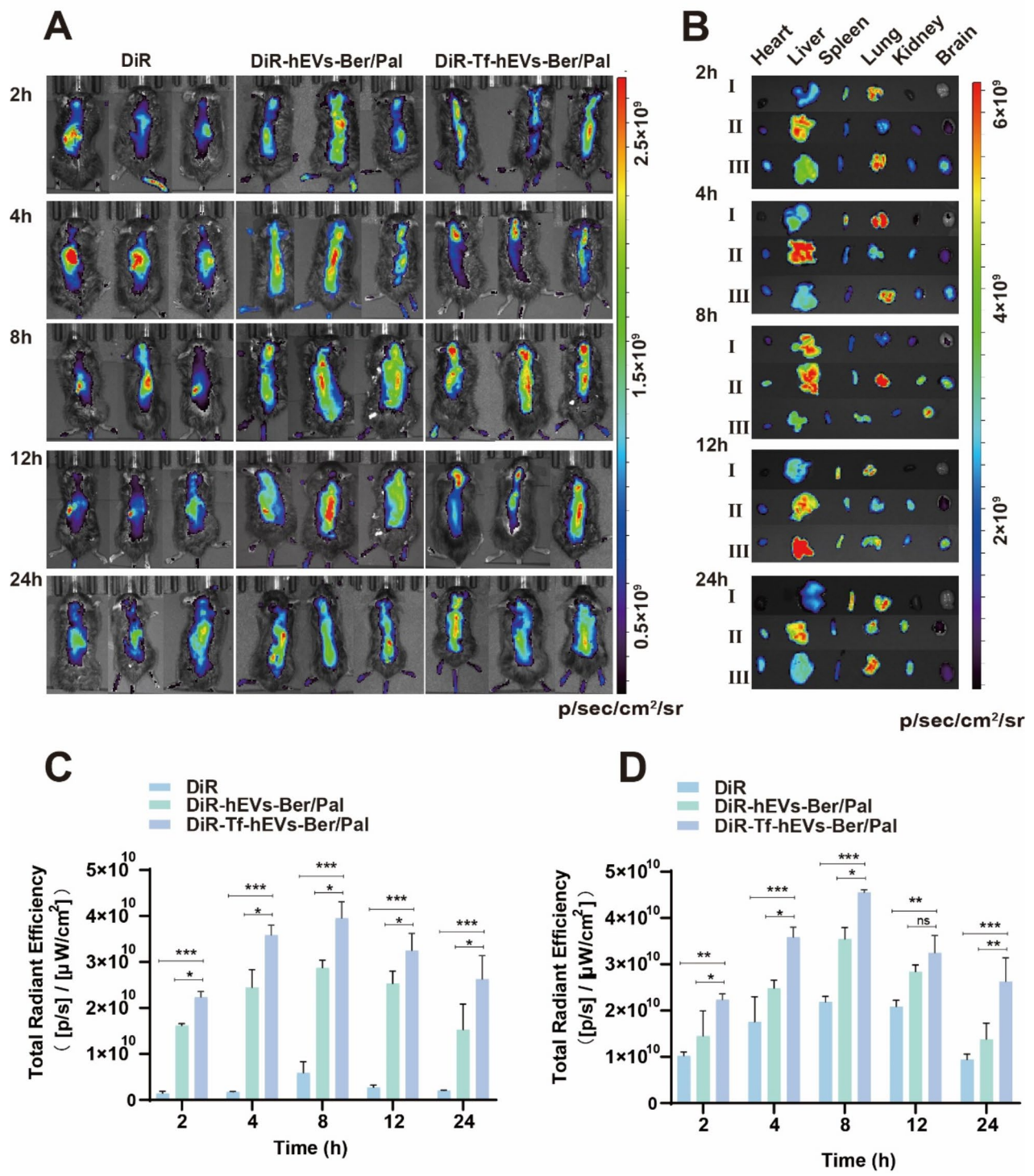


Fig. 5 (See legend on next page.)

(See figure on previous page.)

**Fig. 5** Biological distribution of Tf-hEVs-Ber/Pal in vivo. Representative in vivo fluorescence images of the biodistribution of Tf-hEVs-Ber/Pal (A) in living mice and (B) isolated major tissues (heart, liver, spleen, lung, kidney, and brain) from the mice after 2 h, 4 h, 8 h, 12 h, and 24 h, as detected via an IVIS. I represents DiR, II represents DiR-hEVs-Ber/Pal, and III represents DiR-Tf-hEVs-Ber/Pal. The quantitative average fluorescence intensity (C) within the brain area in the living mice and (D) the isolated brain. The dose of DiR used was 5 mg/kg. The data are presented as the means  $\pm$  SDs ( $n = 3$ ). \* $P < 0.05$ , \*\* $P < 0.01$ , \*\*\* $P < 0.001$ , ns indicates not statistically significant

broad intervention in overall A $\beta$  pathology by this delivery system.

IL-1 $\beta$ , which is secreted by activated microglia, plays a critical role in the amplification of A $\beta$  deposition and neuroinflammation, and its increase is closely associated with neuronal damage and cognitive decline. TNF- $\alpha$  binds to its receptor and activates downstream signaling pathways, promoting the release of proinflammatory mediators. In contrast, IL-4 inhibits the proinflammatory secretion of microglia and induces their polarization to an anti-inflammatory phenotype (M2 microglia). IL-10 is a potent anti-inflammatory factor that exerts neuroprotective effects by inhibiting the nuclear factor kappa-light-chain-enhancer of activated B cells (NF- $\kappa$ B) pathway and inflammatory mediator expression [78–84]. As shown, the expression levels of the proinflammatory cytokines IL-1 $\beta$  and IFN- $\alpha$  were significantly reduced (Fig. 7E and F), whereas the levels of the anti-inflammatory cytokines IL-4 and IL-10 were elevated (Fig. 7G and H). A higher M1/M2 ratio typically reflects a proinflammatory state of microglia, whereas a lower M1/M2 ratio indicates an enhanced anti-inflammatory phenotype, which helps reduce neuroinflammation and neuronal damage. The determination of microglial phenotypes further confirmed the role of Tf-hEVs-Ber/Pal in neuroinflammation in AD mice (Fig. 7I and J). Specifically, the M1/M2 ratio in the TF group was 1.79, which was significantly lower than that in the Ber/Pal group (10.43,  $P < 0.001$ ), hEVs-Ber/Pal (8.93,  $P < 0.001$ ) and single drug loading groups (7.80,  $P < 0.05$ ) indicating that the treatment effectively shifted the phenotype towards the more anti-inflammatory M2 state. (Fig. 7I).

Ber and Pal have been reported to primarily inhibit the NF- $\kappa$ B signaling pathway and the adenosine monophosphate-activated protein kinase (MAPK) signaling pathway to exert anti-inflammatory efficacy [69, 85–89]. Herein, a WB analysis was performed to detect the expression of p38 MAPK and NF- $\kappa$ B p65 in the isolated hippocampus after administration (Fig. S4). In the model group (Saline), both p38 MAPK and NF- $\kappa$ B p65 were significantly upregulated (Fig. S4B–C), indicating a pro-inflammatory state. Notably, compared with Tf-hEVs-Ber and Tf-hEVs-Pal groups, the Tf-hEVs-Ber/Pal group significantly inhibited p38 MAPK expression for 0.5 times and 1 time respectively, and decreased NF- $\kappa$ B p65 expression for 0.5 times and 0.25 times respectively, exhibited more pronounced synergistic inhibitory effects on these two signaling pathways. These results further

confirm that Tf-hEVs-Ber/Pal has strong therapeutic potential for inhibiting neuroinflammation through synergistic effects on multiple pathways [90, 91].

#### Neuroprotective effects of Tf-hEVs-Ber/Pal

The loss of neurons in the hippocampus is closely associated with neuroinflammation and cognitive decline [92–96]. We investigated the neuroprotective effects of Tf-hEVs-Ber/Pal treatment on hippocampal neurons in AD model mice through immunofluorescence staining (Fig. 8). Healthy neuronal cells were stained with Cy3, and the red fluorescence intensity was similar to that of the control mice (Fig. 8A). The quantitative data revealed that the Tf-hEVs-Ber/Pal-treated group presented significantly increased NeuN expression levels (Fig. 8B), indicating the effective inhibition of neuronal loss and apoptosis in the hippocampi of AD model mice. In the Tf-hEVs-Ber/Pal-treated group, the NeuN cell density was significantly greater than that in the Tf-hEVs-Ber and Tf-hEVs-Pal groups, suggesting that the combined treatment has a potential synergistic effect. Compared with that in the saline group, the NeuN cell density in the Tf-hEVs-only group was not significantly decrease, indicating that the Tf-hEVs carrier itself does not induce neurotoxicity or exacerbate neuronal loss. This highlights the safety and efficacy of this nanodelivery platform.

#### In vivo safety evaluation of Tf-hEVs-Ber/Pal

Measuring biochemical indicators in serum samples is a common method to evaluate the safety of novel formulations that provides a comprehensive reflection of the body's health status after treatment. ALT and AST levels are key markers of liver function, and elevated levels often indicate liver damage. CREA and BUN levels are routine indicators for assessing kidney function, and elevated levels may indicate impaired kidney function. ALB and TP levels reflect the body's protein metabolism and overall nutritional status [97, 98]. The results (Fig. 9) revealed no significant differences in these biochemical parameters between the Tf-hEVs-Ber/Pal group and the control group ( $P > 0.05$ ), with all indicators remaining within the normal physiological range, indicating that the administration regimen did not cause noticeable liver or kidney toxicity or metabolic abnormalities. We also performed hematological tests in the serum samples (Table S2). The results revealed no significant differences in any hematological parameters between the Tf-hEVs-Ber/Pal treatment group and the control group ( $P > 0.05$ ), and

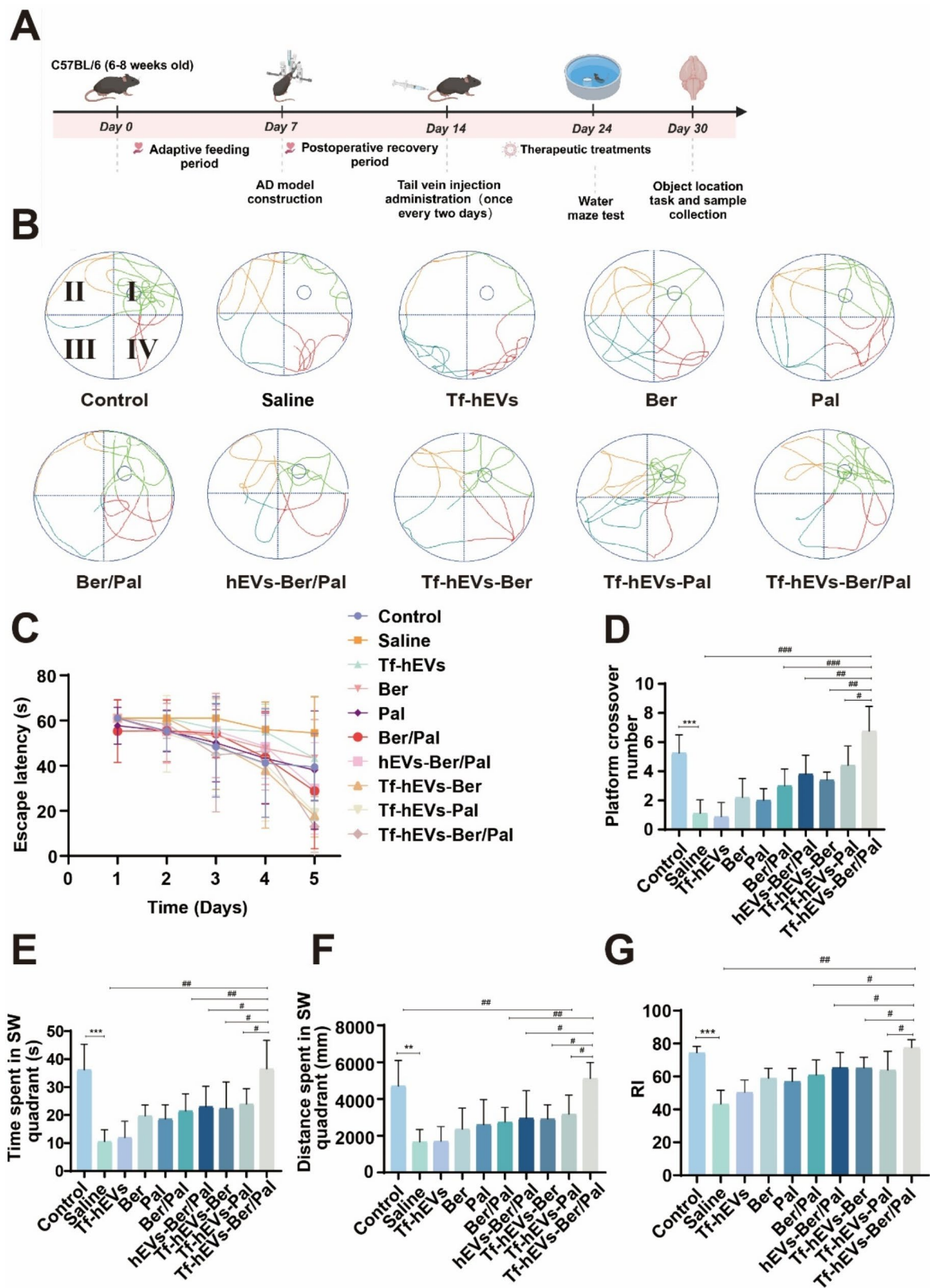


Fig. 6 (See legend on next page.)

(See figure on previous page.)

**Fig. 6** Behavioral improvement in AD model mice after Tf-hEVs-Ber/Pal treatment. **(A)** Diagram of the model construction and therapeutic schedule. **(B)** Trajectories of wild-type and AD mice treated with different preparations in the water maze. Quadrant I is the target quadrant. **(C)** Escape latency time. **(D)** Platform crossing time. **(E)** Target quadrant occupancy in the MWM. and **(F)** target quadrant motion paths. **(G)** NOR performance of mice after administration of different formulations by tail vein injection. RI represents the recognition index. Control indicates wild-type control mice without any intervention. The AD model mice were generated by unilateral injection of the A $\beta$  protein into the hippocampus at an injection dose of 5  $\mu$ M, except for those in the control group. After the model was established, the postoperative recovery time was 1 week, the administration time was 16 days, and the administration interval was once every two days. The dosages of Ber and Pal used were 1.72 and 1.6 mg/kg per mouse, respectively. The data are presented as the means  $\pm$  SDs ( $n=3$ ). Statistical analysis was performed using Student's t test: \* $P < 0.05$ , \*\* $P < 0.01$ , \*\*\* $P < 0.001$ , # $P < 0.05$ , ## $P < 0.01$ , ### $P < 0.001$ , ns, not significant

all the values remained within the normal physiological range. These findings indicate that long-term administration does not induce abnormal immune responses, hematological toxicity, or coagulation issues, further supporting the safety of the Tf-hEVs-Ber/Pal [40, 99].

### Discussion and conclusion

In this work, hybrid vesicles loaded with both Ber and Pal (Tf-hEVs-Ber/Pal) on the basis of Tf-modified liposomes and microglia-derived exosomes were proposed for AD treatment via microglia targeting (Scheme 1). In terms of targeting properties, Tf-hEVs-Ber/Pal exhibited satisfactory brain-targeting ability, which further improved their ability to penetrate the BBB and home to microglia (Figs. 2, 3 and 5). Tf-hEVs-Ber/Pal responded effectively to neuroinflammation related to microglia, increasing the levels of anti-inflammatory cytokines and reducing the secretion of proinflammatory cytokines both in vitro and in vivo, potentially contributing to the M2 polarization of microglia (Figs. 3 and 7). Consequently, after treatment with Tf-hEVs-Ber/Pal in AD model mice, A $\beta$  plaque deposition was reduced (Fig. 7), neuronal damage was alleviated (Fig. 8), and behavioral and cognitive performances were restored (Fig. 6). In summary, Tf-hEVs-Ber/Pal demonstrated potential for treating AD and offered valuable insights for the development of novel nanodrug-mediated brain delivery platforms.

The uncontrollable neuroinflammation induced by microglia, which are resident immune cells in the central nervous system, plays a pivotal role in AD progression [48, 100]. The secreted exosomes of microglia have been reported to be drug carriers capable of targeting microglia and enabling drug delivery to the brain [38, 101–105]. Previously, we optimized extraction methods for microglia-derived Exos and developed a codelivery system based on Exos for AD therapy. However, this system is limited by insufficient drug loading capacity and weak targeting efficiency, which hinders effective microglial targeting and treatment efficacy [95]. These problems were solved by a positive fusion hybrid system decorated with a targeted ligand (Tf in this work), which provides a feasible idea for the development of multifunctional delivery systems characterized by high drug loading and increased targeting. Visibly, the hybrid strategy can effectively

compensate for the shortcomings of a single nanodelivery system.

Ber and Pal, which have been used clinically for many years, are isoquinoline alkaloids and are present in extracts of *Coptis chinensis* and other plants in the genus *Berberis* [106–108]. As patented Chinese medicines, berberine and flavanthen are extensively used for their antibacterial and anti-inflammatory effects and protective effects against infection, and their diverse bioactive properties, including their antioxidant, neuroprotective, anticancer properties and their regulation of glucolipid metabolism, have been studied. In this study, Ber and Pal were coloaded into Tf-hEVs-Ber/Pal for potential synergistic effects, and the results were preliminarily verified. Compared with Tf-hEVs-Ber or Tf-hEVs-Pal, Tf-hEVs-Ber/Pal had more significant therapeutic effects, indicating that the combination of Ber and Pal represents a novel strategy for spatial memory and cognitive function improvements in AD. According to existing studies, Ber directly inhibits  $\beta$ -secretase (BACE1), which is located in the NF- $\kappa$ B downstream pathway, reducing BACE1 expression and decreasing the conversion of amyloid precursor protein (APP) to A $\beta$ . Pal reduces neuroinflammation by modulating NF- $\kappa$ B upstream signaling, promotes M2 microglial polarization, and enhances A $\beta$  phagocytosis and degradation. Therefore, the combined use of Ber and Pal could inhibit the classical inflammatory NF- $\kappa$ B pathway, suppress NF- $\kappa$ B nuclear translocation, and reduce the expression of the downstream proinflammatory mediators IL-1 $\beta$  and TNF- $\alpha$  [69, 71, 86, 109–111].

Antibody therapies and inhibitor treatments for AD have made certain progress, such as donanemab and lecanemab [72, 112–116]. The Tf-hEVs-Ber/Pal, as a novel nanotechnical drug delivery platform, potentially shows synergistic effects with clinical therapy. Antibody therapy mainly targets A $\beta$  plaques, while inhibitor treatments alleviate cognitive impairment by inhibiting acetylcholinesterase or modulating NMDA receptors [117]. However, both approaches fail to address the underlying pathologies of AD, such as neuroinflammation. The Tf-hEVs-Ber/Pal was verified to alleviate neuroinflammation and enhance anti-inflammatory (M2) microglia phenotype transformation. Therefore, combination treatment of the Tf-hEVs-Ber/Pal with clinically used antibodies or inhibitors may improve AD pathology through multiple

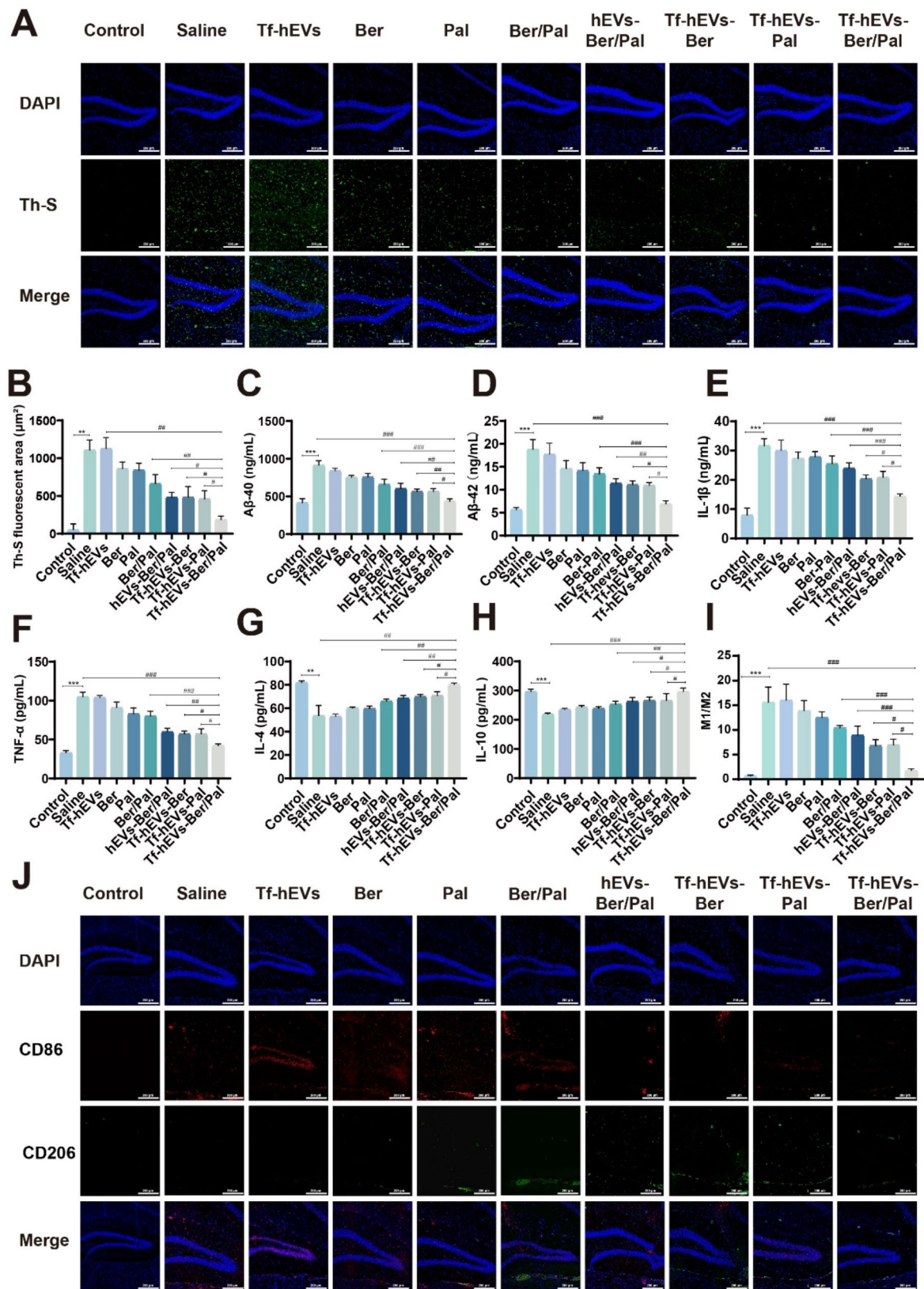


**Fig. 7** (See legend on next page.)

(See figure on previous page.)

**Fig. 7** The anti-AD effects of Tf-hEVs-Ber/Pal include A $\beta$  plaque inhibition, inflammation regulation and microglial phenotype modulation. **(A)** Immunofluorescence staining of the isolated hippocampus was observed using optical microscopy.  $\beta$ -Amyloid plaques were stained with Th-S (green). **(B)** Semi-quantitative data of the green fluorescence signals were analyzed by measuring the average fluorescence intensity using ImageJ. Determination of the concentrations of **(C)** A $\beta$ -40 and **(D)** A $\beta$ -42 with ELISA kits. **(E-H)** The levels of the inflammatory cytokines **(E)** IL-1 $\beta$  and **(F)** TNF- $\alpha$  and the anti-inflammatory cytokines **(G)** IL-4 and **(H)** IL-10 in the isolated hippocampi were measured. Control indicates wild-type control mice without any intervention. **(I)** Semi-quantitative data of CD86 (red) and CD206 (green) signals were analyzed by measuring the average fluorescence intensity via ImageJ, and the M1/M2 ratio was calculated. **(J)** M1 microglia were stained with a PE-conjugated anti-CD86 antibody (red), and M2 microglia were stained with a FITC-conjugated anti-CD206 antibody (green). The cell nuclei were stained with DAPI (blue). Scale bar, 200  $\mu$ m. The AD model mice were generated by unilateral injection of the A $\beta$  protein into the hippocampus at an injection dose of 5  $\mu$ M, except for those in the control group. The data are presented as the means  $\pm$  SDs ( $n=3$ ). Statistical analysis was performed using Student's t test: \* $P<0.05$ , \*\* $P<0.01$ , \*\*\* $P<0.001$ , # $P<0.05$ , ## $P<0.01$ , ### $P<0.001$ , ns, not significant

mechanisms, overall enhancing the therapeutic effect. This multi-target cooperative platform (Tf-hEVs-Ber/Pal) provided a new approach to AD treatment, further promoted the clinical application of Ber and Pal, and offered the potential for comprehensive treatment of AD.

The Tf-hEVs-Ber/Pal developed in this study not only demonstrate superior drug delivery performance in the treatment of AD but also have potential applications in the treatment of other neurodegenerative diseases. For example, in Parkinson's disease (PD) and amyotrophic lateral sclerosis (ALS), excessive activation of

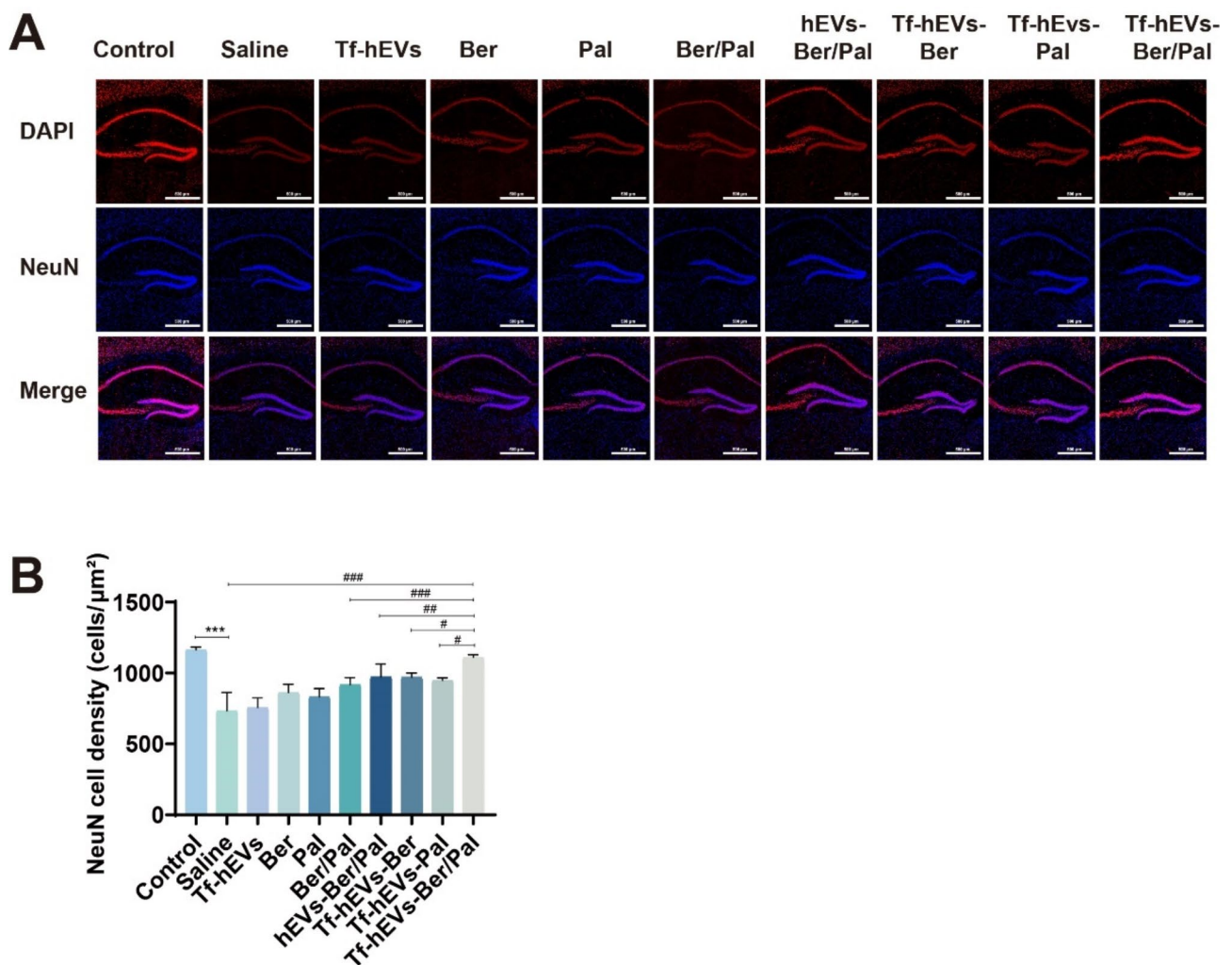


**Fig. 8** Neuronal recovery in AD model mice after Tf-hEVs-Ber/Pal administration. NeuN-positive cells in the hippocampus were **(A)** observed by immunofluorescence staining and **(B)** counted via ImageJ. DAPI is shown in blue, and NeuN is shown in red. Scale bar, 500  $\mu$ m. Control indicates wild-type control mice without any intervention. The AD model mice were generated by unilateral injection of the A $\beta$  protein into the hippocampus at an injection dose of 5  $\mu$ M, except for those in the control group. The data are presented as the means  $\pm$  SDs ( $n=3$ ). Statistical analysis was performed using Student's t test: \* $P<0.05$ , \*\* $P<0.01$ , \*\*\* $P<0.001$ , # $P<0.05$ , ## $P<0.01$ , ### $P<0.001$ , ns, not significant

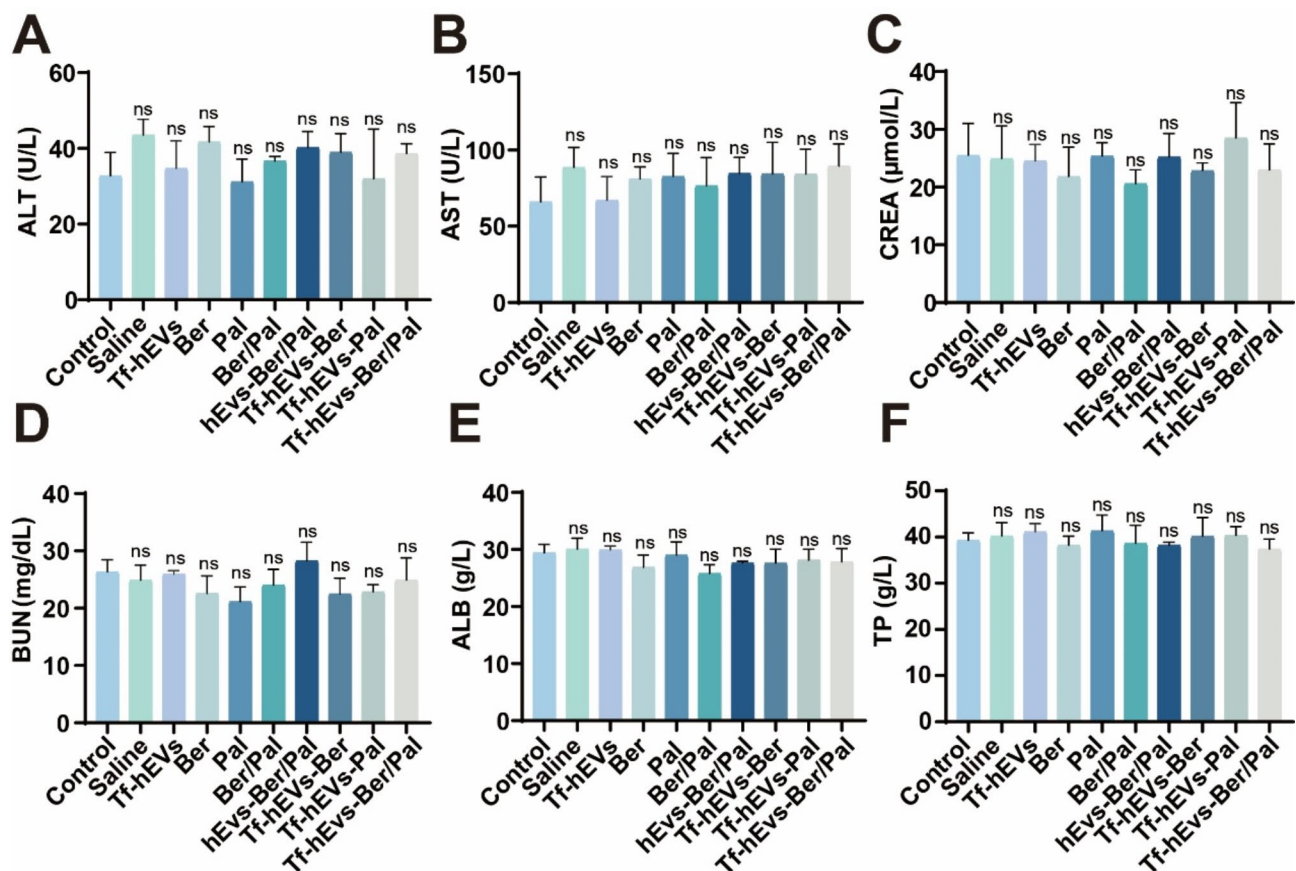


**Fig. 9** Evaluation of the safety of Tf-hEVs-Ber/Pal treatment in AD model mice. (A–F) The levels of ALT, AST, CREA, BUN, ALB, and TP in the serum of AD model mice after therapy were evaluated using biochemical assay kits. The AD model mice were generated by unilateral injection of the A $\beta$  protein into the hippocampus at an injection dose of 5  $\mu$ M, except for those in the control group. The data are presented as the means  $\pm$  SDs ( $n=3$ ). Statistical analysis was performed using Student's t test; ns indicates no significant difference

microglial cells leads to neuronal damage. Tf-hEVs-Ber/Pal achieve efficient BBB penetration, increasing drug delivery to CNS, which helps protect dopaminergic neurons in PD and motor neurons in ALS [118–121]. Additionally, Tf-hEVs-Ber/Pal can target microglial cells and enhance drug accumulation in affected regions, delivering anti-inflammatory drugs (such as Ber and Pal) to regulate neuroinflammation and slow disease progression effectively [122]. Our study provides important experimental evidence for the therapeutic application of Tf-modified hybrid vesicles in AD and other neurodegenerative diseases.

#### Abbreviations

A $\beta$	Amyloid $\beta$
AD	Alzheimer's disease
ALB	Albumin
ALS	Amyotrophic Lateral Sclerosis
ALT	Alanine Aminotransferase
AP	Anterior-Posterior
APP	Amyloid Precursor Protein
ASB	Aspartate Aminotransferase
Ber	Berberine
BV2 cells	Microglia
BUN	Blood Urea Nitrogen

CHOL	Cholesterol
CLSM	Confocal Laser Scanning Microscopy
CREA	Creatinine
DAPI	4'-6-diamidino-2-phenylindole
DiD, 1	1'-dioctadecyl-3,3,3'-tetramethylindodicarbocyanine, 4-chlorobenzenesulfonate salt
DiI, 1	1'-dioctadecyl-3,3,3'-tetramethylindodicarbocyanine perchlorate
DiR, 1	1'-Dioctadecyl-3,3,3'-tetramethylindodicarbocyanine iodide
DLS	Dynamic Light Scattering
DV	Dorsal-Ventral
ELISA	Enzyme-Linked Immunosorbent Assay
Exo	Exosomes
FBS	Fetal Bovine Serum
FCM	Flow Cytometry
FRET	Fluorescence Resonance Energy Transfer
Gran#	Granulocyte Count
Gran%	Granulocyte Percentage
HCT	Hematocrit
HGB	Hemoglobin
HIF-1 $\alpha$	Hypoxia-Inducible Factor 1 Alpha
hEVs	Hybrid nano extracellular vesicles
HPLC	High-Performance Liquid Chromatography
HSPC	Hydrogenated Soybean Phosphatidylcholine
HEK293	Human Embryonic Kidney 293 Cells
IL-1 $\beta$	Interleukin 1 beta
IVIS	In Vivo Imaging System
LPS	Lipopolysaccharide

Lymph#	Lymphocyte count
Lymph%	Lymphocyte Percentage
MCH	Mean Corpuscular Hemoglobin
MCHC	Mean Corpuscular Hemoglobin Concentration
MCV	Mean Corpuscular Volume
ML	Medial-Lateral
Mon#	Monocyte Count
Mon%	Monocyte Percentage
MPV	Mean Platelet Volume
MWM	Morris Water Maze
mTOR	Mechanistic Target of Rapamycin
NC	Nitrocellulose
NF-κB	Nuclear Factor Kappa-Light-Chain-Enhancer of Activated B cells
NO	Nitric Oxide
NOR	Novel Object Recognition
Pal	Palmitate
PBS	Phosphate-Buffered Saline
PDI	Polydispersity Index
PFA	Paraformaldehyde
PD	Parkinson's Disease
PDW	Platelet Distribution Width
PLT	Platelet Count
RBC	Red Blood Cell Count
RDW	Red Cell Distribution Width
RI	Recognition Index
SDS-PAGE	Sodium Dodecyl Sulfate-Polyacrylamide Gel Electrophoresis
TCA	Tricarboxylic Acid
TEM	Transmission Electron Microscopy
TEER	Trans-Epithelial Electrical Resistance
Tf	Transferrin
Tf-hEVs	Tf-Modified hybrid vesicles
Tf-hEVs-Ber	Tf-Modified Hybrid Vesicles Loaded with Berberine
Tf-hEVs-Ber/Pal	Tf-Modified Hybrid Vesicles Co-Loaded with Berberine and Palmitate
Tf-Lip-Ber	Berberine-Loaded Tf-Modified Liposomes
TfR	Transferrin Receptor
TNF-α	Tumor Necrosis Factor Alpha
TP	Total Protein
WB	Western Blot
WBC	White Blood Cell Count

## Supplementary Information

The online version contains supplementary material available at <https://doi.org/10.1186/s12951-025-03385-z>.

Supplementary Material 1

Supplementary Material 2

## Author contributions

Peng Zhou conducted the research, analyzed the data, wrote the manuscript, and served as the first author. Quan Cao and Chen Li assisted with the preparation of the process and cell experiments. NingJing Wang and Siqi Guo contributed to the data analysis. Pingping Wang, Pingyuan Ge, and Caihong Li assisted with the animal experiments. This research idea was proposed by Qingqing Xiao, who revised the entire manuscript. Huaxu Zhu funded all of the experiments. All authors approved the final version of the manuscript.

## Funding

This study was supported by the National Natural Science Foundation of China (No. 82274222), the Natural Science Foundation Project of Jiangsu Province (No. BK20230463), and the Jiangsu Province Leading Talents Cultivation Project for Traditional Chinese Medicine (SLJ0304).

## Data availability

No datasets were generated or analysed during the current study.

## Declarations

### Ethics approval and consent to participate

Animal handling and surgical operations were carried out in accordance with protocols approved by the Ethics Committee of Nanjing University of Chinese Medicine, Ethics number: 202303A016.

### Competing interests

The authors declare no competing interests.

### Author details

<sup>1</sup>Jiangsu Botanical Medicine Refinement Engineering Research Center, Nanjing University of Chinese Medicine, Nanjing 210023, China

<sup>2</sup>State Key Laboratory of Research & Development of Characteristic Qin Medicine Resources, Shannxi University of Chinese Medicine, Xianyang 712038, China

<sup>3</sup>China Academy of Chinese Medical Sciences, Beijing 100700, China

<sup>4</sup>Polymer Science and Materials Chemistry, Exponent Ltd, Hong Kong 999077, China

Received: 27 January 2025 / Accepted: 11 April 2025

Published online: 24 April 2025

## References

- O'Keeffe M, Booker SA, Walsh D, Li M, Henley C, Simões de Oliveira L, Liu M, Wang X, Banqueri M, Ridley K, et al. Typical development of synaptic and neuronal properties can proceed without microglia in the cortex and thalamus. *Nat Neurosci*. 2025;28(2):268–79.
- Baligács N, Albertini G, Borrie SC, Serneels L, Pridans C, Balusu S, De Strooper B. Homeostatic microglia initially seed and activated microglia later reshape amyloid plaques in Alzheimer's disease. *Nat Commun*. 2024;15(1):10634.
- Geloso MC, Zupo L, Corvino V. Crosstalk between peripheral inflammation and brain: focus on the responses of microglia and astrocytes to peripheral challenge. *Neurochem Int*. 2024;180:105872.
- Bernier LP, York EM, MacVicar BA. Immunometabolism in the brain: how metabolism shapes microglial function. *Trends Neurosci*. 2020;43(11):854–69.
- Sun N, Victor MB, Park YP, Xiong X, Scannail AN, Leary N, Prosper S, Viswanathan S, Luna X, Boix CA, et al. Human microglial state dynamics in Alzheimer's disease progression. *Cell*. 2023;186(20):4386–e44034329.
- Xu X, He Y, Liu J, Berberine. A multifaceted agent for lung cancer treatment—from molecular insight to clinical applications. *Gene*. 2025;934:149021.
- Jiang Y-J, Cheng Y-H, Zhu H-Q, Wu Y-L, Nan J-X, Lian L-H. Palmitate, an isoquinoline alkaloid from *Phellodendron amurense* Rupr., ameliorated gouty inflammation by inhibiting pyroptosis via NLRP3 inflammasome. *J Ethnopharmacol*. 2025;340:119231.
- Wu D, Chen Q, Chen X, Han F, Chen Z, Wang Y. The blood–brain barrier: structure, regulation and drug delivery. *Signal Transduct Target Ther*. 2023;8(1):217.
- Li X, Zou J, He Z, Sun Y, Song X, He W. The interaction between particles and vascular endothelium in blood flow. *Adv Drug Del Rev*. 2024;207:115216.
- Ashique S, Pal R, Sharma H, Mishra N, Garg A. Unraveling the emerging niche role of extracellular vesicles (EVs) in traumatic brain injury (TBI). *CNS Neurol Disord Drug Targets*. 2024;23(11):1357–70.
- Wang P, Wang Y, Li P, Chen C, Ma S, Zhao L, He H, Yin T, Zhang Y, Tang X, Gou J. Oral delivery of polyester nanoparticles for brain-targeting: challenges and opportunities. *Chin Chem Lett*. 2023;34(4):107691.
- Yang Z, Shi J, Xie J, Wang Y, Sun J, Liu T, Zhao Y, Zhao X, Wang X, Ma Y, et al. Large-scale generation of functional mRNA-encapsulating exosomes via cellular nanoporation. *Nat Biomed Eng*. 2020;4(1):69–83.
- Soltanmohammadi F, Gharehbabaa AM, Zangi AR, Adibkia K, Javadzadeh Y. Current knowledge of hybrid nanoplatforms composed of exosomes and organic/inorganic nanoparticles for disease treatment and cell/tissue imaging. *Biomed Pharmacother*. 2024;178:117248.
- Palakurthi SS, Shah B, Kapre S, Charbe N, Immanuel S, Pasham S, Thalla M, Jain A, Palakurthi S. A comprehensive review of challenges and advances in exosome-based drug delivery systems. *Nanoscale Adv*. 2024;6(23):5803–26.
- Song X, Gu L, Yang Q, Wu J, Chen J, Tian X, Sun L, Chen L. Thermosensitive injectable hydrogel loaded with hypoxia-induced exosomes maintains chondrocyte phenotype through NDRG3-mediated hypoxic response. *Chin Chem Lett*. 2023;34(8):108079.

16. Xiao Q, Li X, Liu C, Yang Y, Hou Y, Wang Y, Su M, He W. Liposome-based anchoring and core-encapsulation for combinatorial cancer therapy. *Chin Chem Lett.* 2022;33(9):4191–6.
17. Xiao Q, Li X, Liu C, Jiang Y, He Y, Zhang W, Azevedo HS, Wu W, Xia Y, He W. Improving cancer immunotherapy via co-delivering checkpoint blockade and thrombospondin-1 downregulator. *Acta Pharm Sin B.* 2023;13(8):3503–17.
18. Yuan J, Guo M, Zhao S, Li J, Wang X, Yang J, Jin Z, Song X. Core-shell lipid-polymeric nanoparticles for enhanced oral bioavailability and antihypertensive efficacy of KY5 peptide. *Chin Chem Lett.* 2023;34(4):107943.
19. Wang T, Fu Y, Sun S, Huang C, Yi Y, Wang J, Deng Y, Wu M. Exosome-based drug delivery systems in cancer therapy. *Chin Chem Lett.* 2023;34(2):107508.
20. Hao X, Gan J, Cao J, Zhang D, Liang J, Sun L. Biomimetic liposomes hybrid with erythrocyte membrane modulate dendritic cells to ameliorate systemic lupus erythematosus. *Mater Today Bio.* 2023;20:100625.
21. Geng T, Tang M, Yee Paek S, Leung E, Chamley LW, Wu Z. A simple approach to re-engineering small extracellular vesicles to circumvent endosome entrapment. *Int J Pharm.* 2022;626:122153.
22. Sharma H, Rachamalla HK, Mishra N, Chandra P, Pathak R, Ashique S. Introduction to exosome and its role in brain disorders. Singapore: Springer; 2024.
23. Kumar P, Sharma H, Singh A, Pandey SN, Chandra P. Correlation between exosomes and Neuro-inflammation in various brain disorders. Singapore: Springer; 2024.
24. Sharma H, Anand A, Halagali P, Inamdar A, Pathak R, Taghizadeh-Hesary F, Ashique S. Role of flavonoids in chronic metabolic diseases. Scrivener Publishing; 2024.
25. Sharma H, Tyagi SJ, Chandra P, Verma A, Kumar P, Ashique S, Hussain A. Exosomes based drug delivery strategies for brain disorders. Singapore: Springer; 2024.
26. Liu Y, Zhu M, Meng M, Wang Q, Wang Y, Lei Y, Zhang Y, Weng L, Chen X. A dual-responsive hyaluronic acid nanocomposite hydrogel drug delivery system for overcoming multiple drug resistance. *Chin Chem Lett.* 2023;34(1):107583.
27. Zhu H, Yu J, Ye J, Wu Y, Pan J, Li Y, Chen C, Zheng L, Liu G, Chu C. Nanoparticle-mediated corneal neovascularization treatments: toward new generation of drug delivery systems. *Chin Chem Lett.* 2023;34(3):107648.
28. Wang X, Chen S, Xia X, Du Y, Wei Y, Yang W, Zhang Y, Song Y, Lei T, Huang Q, Gao H. Lysosome-Targeting protein degradation through endocytosis pathway triggered by polyvalent Nano-Chimera for AD therapy. *Adv Mater.* 2025;37(5):e2411061.
29. Zare D, Rajizadeh MA, Maneshian M, Jonaidi H, Sheibani V, Asadi-Shekaari M, Yousefi M, Esmailpour K. Inhibition of protease-activated receptor 1 (PAR1) ameliorates cognitive performance and synaptic plasticity impairments in animal model of Alzheimer's diseases. *Psychopharmacology.* 2021;238(6):1645–56.
30. Yan XS, Yang ZJ, Jia JX, Song W, Fang X, Cai ZP, Huo DS, Wang H. Protective mechanism of testosterone on cognitive impairment in a rat model of Alzheimer's disease. *Neural Regen Res.* 2019;14(4):649–57.
31. Kapoor KS, Harris K, Arian KA, Ma L, Schueng Zancanela B, Church KA, McAndrews KM, Kalluri R. High throughput and rapid isolation of extracellular vesicles and exosomes with purity using size exclusion liquid chromatography. *Bioact Mater.* 2024;40:683–95.
32. Takov K, Yellon DM, Davidson SM. Comparison of small extracellular vesicles isolated from plasma by ultracentrifugation or size-exclusion chromatography: yield, purity and functional potential. *J Extracell Vesicles.* 2019;8(1):1560809.
33. Li W, Li C, Zhou T, Liu X, Liu X, Li X, Chen D. Role of Exosomal proteins in cancer diagnosis. *Mol Cancer.* 2017;16(1):145.
34. Fernandes M, Lopes I, Magalhaes L, Sarria MP, Machado R, Sousa JC, Botelho C, Teixeira J, Gomes AC. Novel concept of exosome-like liposomes for the treatment of Alzheimer's disease. *J Control Release.* 2021;336:130–43.
35. Ha D, Yang N, Nadithe V. Exosomes as therapeutic drug carriers and delivery vehicles across biological membranes: current perspectives and future challenges. *Acta Pharm Sin B.* 2016;6(4):287–96.
36. Mondal J, Pillarisetti S, Junnuthula V, Saha M, Hwang SR, Park IK, Lee YK. Hybrid exosomes, exosome-like nanovesicles and engineered exosomes for therapeutic applications. *J Control Release.* 2023;353:1127–49.
37. Mukherjee A, Bisht B, Dutta S, Paul MK. Current advances in the use of exosomes, liposomes, and bioengineered hybrid nanovesicles in cancer detection and therapy. *Acta Pharmacol Sin.* 2022;43(11):2759–76.
38. Li YJ, Wu JY, Liu J, Xu W, Qiu X, Huang S, Hu XB, Xiang DX. Artificial exosomes for translational nanomedicine. *J Nanobiotechnol.* 2021;19(1):242.
39. Piffoux M, Silva AKA, Wilhelm C, Gazeau F, Tareste D. Modification of extracellular vesicles by fusion with liposomes for the design of personalized biogenic drug delivery systems. *ACS Nano.* 2018;12(7):6830–42.
40. Lv Q, Cheng L, Lu Y, Zhang X, Wang Y, Deng J, Zhou J, Liu B, Liu J. Thermosensitive Exosome-Liposome hybrid Nanoparticle-Mediated chemioimmunotherapy for improved treatment of metastatic peritoneal Cancer. *Adv Sci (Weinh).* 2020;7(18):2000515.
41. Lebreton V, Kaeokhamloed N, Vasyilaki A, Hilairat G, Mellinger A, Béjaud J, Saulnier P, Lagarce F, Gattacceca F, Legeay S, Roger E. Pharmacokinetics of intact lipid nanocapsules using new quantitative FRET technique. *J Control Release.* 2022;351:681–91.
42. Chen T, He B, Tao J, He Y, Deng H, Wang X, Zheng Y. Application of Förster resonance energy transfer (FRET) technique to elucidate intracellular and in vivo biofate of nanomedicines. *Adv Drug Del Rev.* 2019;143:177–205.
43. Zhang H, Pan Y, Li Y, Tang C, Xu Z, Li C, Xu F, Mai Y. Hybrid polymer vesicles: controllable Preparation and potential applications. *Biomacromolecules.* 2023;24(9):3929–53.
44. Moholkar DN, Kandimalla R, Gupta RC, Aqil F. Advances in lipid-based carriers for cancer therapeutics: liposomes, exosomes and hybrid exosomes. *Cancer Lett.* 2023;565:216220.
45. Ashby G, Keng KE, Hayden CC, Gollapudi S, Houser JR, Jamal S, Stachowiak JC. Selective endocytic uptake of targeted liposomes occurs within a narrow range of liposome diameters. *ACS Appl Mater Interfaces.* 2023;15(43):49988–50001.
46. Gandek TB, van der Koog L, Nagelkerke A. A comparison of cellular uptake mechanisms, delivery efficacy, and intracellular fate between liposomes and extracellular vesicles. *Adv Healthc Mater.* 2023;12(25):e2300319.
47. Samson LD. A target to suppress inflammation. *Science.* 2018;362(6416):748–9.
48. Hurlley SM. A microglia type associated with AD. *Science.* 2017;357(6347):160–1.
49. Ji Z, Liu C, Zhao W, Soto C, Zhou X. Multi-scale modeling for systematically understanding the key roles of microglia in AD development. *Comput Biol Med.* 2021;133:104374.
50. Sayed FA, Kodama L, Fan L, Carling GK, Udeochu JC, Le D, Li Q, Zhou L, Wong MY, Horowitz R, et al. AD-linked R47H-TREM2 mutation induces disease-enhancing microglial States via AKT hyperactivation. *Sci Transl Med.* 2021;13(622):eabe3947.
51. Leng F, Edison P. Neuroinflammation and microglial activation in Alzheimer disease: where do we go from here? *Nat Rev Neurol.* 2021;17(3):157–72.
52. Wei Y, Sun Y, Wei J, Qiu X, Meng F, Storm G, Zhong Z. Selective transferrin coating as a facile strategy to fabricate BBB-permeable and targeted vesicles for potent RNAi therapy of brain metastatic breast cancer in vivo. *J Control Release.* 2021;337:521–9.
53. Shimbo T, Kawachi M, Saga K, Fujita H, Yamazaki T, Tamai K, Kaneda Y. Development of a transferrin receptor-targeting HVJ-E vector. *Biochem Biophys Res Commun.* 2007;364(3):423–8.
54. Goswami U, Dutta A, Raza A, Kandimalla R, Kalita S, Ghosh SS, Chattopadhyay A. Transferrin-Copper Nanocluster-Doxorubicin nanoparticles as targeted theranostic Cancer nanodrug. *ACS Appl Mater Interfaces.* 2018;10(4):3282–94.
55. Fan K, Zhou M, Yan X. Questions about horse spleen ferritin crossing the blood brain barrier via mouse transferrin receptor 1. *Protein Cell.* 2017;8(11):788–90.
56. Tomatis F, Rosa S, Simões S, Barão M, Jesus C, Novo J, Barth E, Marz M, Ferreira L. Engineering extracellular vesicles to transiently permeabilize the blood-brain barrier. *J Nanobiotechnol.* 2024;22(1):747.
57. Liu D, Ji Q, Cheng Y, Liu M, Zhang B, Mei Q, Huan M, Zhou S. Cyclosporine A loaded brain targeting nanoparticle to treat cerebral ischemia/reperfusion injury in mice. *J Nanobiotechnol.* 2022;20(1):256.
58. Zhou Y, Zhou W, Chen X, Wang Q, Li C, Chen Q, Zhang Y, Lu Y, Ding X, Jiang C. Bone marrow mesenchymal stem cells-derived exosomes for penetrating and targeted chemotherapy of pancreatic cancer. *Acta Pharm Sin B.* 2020;10(8):1563–75.
59. Kafa H, Wang JT, Rubio N, Klippstein R, Costa PM, Hassan HA, Sosabowski JK, Bansal SS, Preston JE, Abbott NJ, Al-Jamal KT. Translocation of LRP1 targeted carbon nanotubes of different diameters across the blood-brain barrier in vitro and in vivo. *J Control Release.* 2016;225:217–29.
60. Xu M, Soliman MG, Sun X, Pelaz B, Feliu N, Parak WJ, Liu S. How entanglement of different physicochemical properties complicates the prediction of in vitro and in vivo interactions of gold nanoparticles. *ACS Nano.* 2018;12(10):10104–13.

61. Sonali, Singh RP, Singh N, Sharma G, Vijayakumar MR, Koch B, Singh S, Singh U, Dash D, Pandey BL, Muthu MS. Transferrin liposomes of docetaxel for brain-targeted cancer applications: formulation and brain theranostics. *Drug Deliv*. 2016;23(4):1261–71.
62. Gopalan D, Pandey A, Udupa N, Mutalik S. Receptor specific, stimuli responsive and subcellular targeted approaches for effective therapy of Alzheimer: role of surface engineered nanocarriers. *J Control Release*. 2020;319:183–200.
63. Wan M, Sun S, Di X, Zhao M, Lu F, Zhang Z, Li Y. Icaritin improves learning and memory function in Abeta(1–42)-induced AD mice through regulation of the BDNF-TrkA signaling pathway. *J Ethnopharmacol*. 2024;318(Pt B):117029.
64. Bolmont T, Clavaguera F, Meyer-Luehmann M, Herzog MC, Radde R, Staufenbiel M, Lewis J, Hutton M, Tolnay M, Jucker M. Induction of Tau pathology by intracerebral infusion of amyloid-beta-containing brain extract and by amyloid-beta deposition in APP X Tau Transgenic mice. *Am J Pathol*. 2007;171(6):2012–20.
65. Hour FQ, Moghadam AJ, Shakeri-Zadeh A, Bakhtiyari M, Shabani R, Mehdizadeh M. Magnetic targeted delivery of the SPIONs-labeled mesenchymal stem cells derived from human Wharton's jelly in Alzheimer's rat models. *J Control Release*. 2020;321:430–41.
66. Chen Q, Du Y, Zhang K, Liang Z, Li J, Yu H, Ren R, Feng J, Jin Z, Li F, et al. Tau-Targeted multifunctional nanocomposite for combinational therapy of Alzheimer's disease. *ACS Nano*. 2018;12(2):1321–38.
67. Shi Y, Huang W, Wang Y, Zhang R, Hou L, Xu J, Qiu Z, Xie Q, Chen H, Zhang Y, Wang H. Bis(9)-(-)-Meptazinol, a novel dual-binding ache inhibitor, rescues cognitive deficits and pathological changes in APP/PS1 Transgenic mice. *Transl Neurodegener*. 2018;7:21.
68. Qi YY, Heng X, Yao ZY, Qu SY, Ge PY, Zhao X, Ni SJ, Guo R, Yang NY, Zhang QC, Zhu HX. Involvement of Huanglian Jiedu Decoction on microglia with abnormal sphingolipid metabolism in Alzheimer's disease. *Drug Des Devel Ther*. 2022;16:931–50.
69. Zeng J, Pei H, Wu H, Chen W, Du R, He Z. Palmatine attenuates LPS-induced neuroinflammation through the PI3K/Akt/NF-kappaB pathway. *J Biochem Mol Toxicol*. 2024;38(1):e23544.
70. Xu Y, Shen B, Pan X, Liu C, Wang Y, Chen X, Wang T, Chen G, Chen J. Palmatine ameliorated lipopolysaccharide-induced sepsis-associated encephalopathy mice by regulating the microbiota-gut-brain axis. *Phytomedicine*. 2024;124:155307.
71. Wang K, Yin J, Chen J, Ma J, Si H, Xia D. Inhibition of inflammation by Berberine: molecular mechanism and network Pharmacology analysis. *Phytomedicine*. 2024;128:155258.
72. Zhu K, Yao Y, Wang K, Shao F, Zhu Z, Song Y, Zhou Z, Jiang D, Lan X, Qin C. Berberin sustained-release nanoparticles were enriched in infarcted rat myocardium and resolved inflammation. *J Nanobiotechnol*. 2023;21(1):33.
73. Xia Y, Wang X, Lin S, Dong TTX, Tsim KWK. Berberine and palmatine, acting as allosteric potential ligands of alpha7 nAChR, synergistically regulate inflammation and phagocytosis of microglial cells. *FASEB J*. 2024;38(19):e70094.
74. Ding MR, Qu YJ, Hu B, An HM. Signal pathways in the treatment of Alzheimer's disease with traditional Chinese medicine. *Biomed Pharmacother*. 2022;152:113208.
75. Durairajan SSK, Iyaswamy A, Shetty SG, Kammella AK, Malampati S, Shang W, Yang C, Song J, Chung S, Huang J, et al. A modified formulation of Huanglian-Jie-Du-Tang reduces memory impairments and beta-amyloid plaques in a triple Transgenic mouse model of Alzheimer's disease. *Sci Rep*. 2017;7(1):6238.
76. Iyaswamy A, Wang X, Krishnamoorthi S, Kaliamoorthy V, Sreenivasurthy SG, Kumar Durairajan SS, Song JX, Tong BC, Zhu Z, Su CF, et al. Theranostic F-SLOH mitigates Alzheimer's disease pathology involving TFEB and ameliorates cognitive functions in Alzheimer's disease models. *Redox Biol*. 2022;51:102280.
77. Starling S. Alzheimer disease: Blood-derived Abeta induces AD pathology. *Nat Rev Neurol*. 2018;14(1):2.
78. Bettcher BM, Tansey MG, Dorothee G, Heneka MT. Peripheral and central immune system crosstalk in alzheimer disease - a research prospectus. *Nat Rev Neurol*. 2021;17(11):689–701.
79. Yang F, Zhao K, Zhang X, Zhang J, Xu B. ATP induces disruption of tight junction proteins via IL-1 Beta-Dependent MMP-9 activation of human Blood-Brain barrier in vitro. *Neural Plast*. 2016;2016:8928530.
80. Botella Lucena P, Heneka MT. Inflammatory aspects of Alzheimer's disease. *Acta Neuropathol*. 2024;148(1):31.
81. Heneka MT, van der Flier WM, Jessen F, Hoozemans J, Thal DR, Boche D, Brosseron F, Teunissen C, Zetterberg H, Jacobs AH et al. Neuroinflammation in alzheimer disease. *Nat Rev Immunol*. 2024.
82. Xu C, Wu J, Wu Y, Ren Z, Yao Y, Chen G, Fang EF, Noh JH, Liu YU, Wei L, et al. TNF-alpha-dependent neuronal necroptosis regulated in Alzheimer's disease by coordination of RIPK1-p62 complex with autophagic UVRAG. *Theranostics*. 2021;11(19):9452–69.
83. Asby D, Boche D, Allan S, Love S, Miners JS. Systemic infection exacerbates cerebrovascular dysfunction in Alzheimer's disease. *Brain*. 2021;144(6):1869–83.
84. Hansen DV, Hanson JE, Sheng M. Microglia in Alzheimer's disease. *J Cell Biol*. 2018;217(2):459–72.
85. Xiao T, Yu X, Yang L, Duan X. Palmatine treats urticaria by reducing inflammation and increasing autophagy. *Front Immunol*. 2023;14:1268467.
86. Lin X, Zhang N, Berberine. Pathways to protect neurons. *Phytother Res*. 2018;32(8):1501–10.
87. Liu T, Zhang L, Joo D, Sun SC. NF-kappaB signaling in inflammation. *Signal Transduct Target Ther*. 2017;2:17023.
88. Lingappan K. NF-kappaB in oxidative stress. *Curr Opin Toxicol*. 2018;7:81–6.
89. Sharma H, Chandra P, Challenges, Prospects F. A benefaction of phytoconstituents on molecular targets pertaining to Alzheimer's disease. *Int J Pharm Investig*. 2023;14(1):117–26.
90. Sun SC. The non-canonical NF-kappaB pathway in immunity and inflammation. *Nat Rev Immunol*. 2017;17(9):545–58.
91. Cao M, Day AM, Galler M, Latimer HR, Byrne DP, Foy TW, Dwyer E, Bennett E, Palmer J, Morgan BA, et al. A peroxiredoxin-P38 MAPK scaffold increases MAPK activity by MAP3K-independent mechanisms. *Mol Cell*. 2023;83(17):3140–e31543147.
92. Leng K, Li E, Eser R, Piergies A, Sit R, Tan M, Neff N, Li SH, Rodriguez RD, Suetomoto CK, et al. Molecular characterization of selectively vulnerable neurons in Alzheimer's disease. *Nat Neurosci*. 2021;24(2):276–87.
93. Howard R, Kales HC. New treatments for Alzheimer's disease. *BMJ*. 2023;382:1852.
94. Henstridge CM, Hyman BT, Spires-Jones TL. Beyond the neuron-cellular interactions early in alzheimer disease pathogenesis. *Nat Rev Neurosci*. 2019;20(2):94–108.
95. Zhao X, Ge P, Lei S, Guo S, Zhou P, Zhao L, Qi Y, Wei X, Wu W, Wang N, et al. An Exosome-Based therapeutic strategy targeting neuroinflammation in Alzheimer's disease with Berberine and palmatine. *Drug Des Devel Ther*. 2023;17:2401–20.
96. Tzioras M, McGeachan RI, Durrant CS, Spires-Jones TL. Synaptic degeneration in alzheimer disease. *Nat Rev Neurol*. 2023;19(1):19–38.
97. Zhou X, Miao Y, Wang Y, He S, Guo L, Mao J, Chen M, Yang Y, Zhang X, Gan Y. Tumour-derived extracellular vesicle membrane hybrid lipid nanovesicles enhance siRNA delivery by tumour-homing and intracellular freeway transportation. *J Extracell Vesicles*. 2022;11(3):e12198.
98. Li L, He D, Guo Q, Zhang Z, Ru D, Wang L, Gong K, Liu F, Duan Y, Li H. Exosome-liposome hybrid nanoparticle codelivery of TP and miR497 conspicuously overcomes chemoresistant ovarian cancer. *J Nanobiotechnol*. 2022;20(1):50.
99. Kawabata H. Transferrin and transferrin receptors update. *Free Radic Biol Med*. 2019;133:46–54.
100. Bassil R, Shields K, Granger K, Zein I, Ng S, Chih B. Improved modeling of human AD with an automated culturing platform for iPSC neurons, astrocytes and microglia. *Nat Commun*. 2021;12(1):5220.
101. Song Y, Li Z, He T, Qu M, Jiang L, Li W, Shi X, Pan J, Zhang L, Wang Y, et al. M2 microglia-derived exosomes protect the mouse brain from ischemia-reperfusion injury via Exosomal miR-124. *Theranostics*. 2019;9(10):2910–23.
102. Jeppesen DK, Fenix AM, Franklin JL, Higginbotham JN, Zhang Q, Zimmerman LJ, Liebler DC, Ping J, Liu Q, Evans R, et al. Reassessment Exosome Composition Cell. 2019;177(2):428–e445418.
103. Xiao T, Zhang W, Jiao B, Pan CZ, Liu X, Shen L. The role of exosomes in the pathogenesis of Alzheimer' disease. *Transl Neurodegener*. 2017;6:3.
104. Cui J, Wang X, Li J, Zhu A, Du Y, Zeng W, Guo Y, Di L, Wang R. Immune exosomes loading Self-Assembled nanomicelles traverse the Blood-Brain barrier for Chemo-immunotherapy against glioblastoma. *ACS Nano*. 2023.
105. Sharma H, Rani T, Khan S. An insight into neuropathic pain: A systemic and Up-to-date review. *Int J Pharm Sci*. 2023;14(2):607–21.
106. Imenshahidi M, Hosseinzadeh H. Berberine and barberry (*Berberis vulgaris*): A clinical review. *Phytother Res*. 2019;33(3):504–23.
107. Ekeku SO, Pang KL, Chin KY. Palmatine as an agent against metabolic syndrome and its related complications: A review. *Drug Des Devel Ther*. 2020;14:4963–74.

108. Halagali P, Inamdar A, Singh J, Anand A, Sadhu P, Pathak R, Sharma H, Biswas D. Phytochemicals, herbal extracts, and dietary supplements for metabolic disease management. *Endocr Metab Immune Disord Drug Targets*; 2024.
109. Wang Y, Pei H, Chen W, Du R, Li J, He Z. Palmatine protects PC12 cells and mice from Abeta25-35-Induced oxidative stress and neuroinflammation via the Nrf2/HO-1 pathway. *Molecules*. 2023; 28(24).
110. Cheng Z, Kang C, Che S, Su J, Sun Q, Ge T, Guo Y, Lv J, Sun Z, Yang W, et al. Berberine: A promising treatment for neurodegenerative diseases. *Front Pharmacol*. 2022;13:845591.
111. Akbar M, Shabbir A, Rehman K, Akash MSH, Shah MA. Neuroprotective potential of Berberine in modulating Alzheimer's disease via multiple signaling pathways. *J Food Biochem*. 2021;45(10):e13936.
112. Kapoor DU, Sharma H, Maheshwari R, Pareek A, Gaur M, Prajapati BG, Castro GR, Thanawuth K, Suttiruengwong S, Sriamornsak P. Konjac Glucomannan: A comprehensive review of its extraction, health benefits, and pharmaceutical applications. *Carbohydr Polym*. 2024;339:122266.
113. Cummings J. Anti-Amyloid monoclonal antibodies are transformative treatments that redefine Alzheimer's disease therapeutics. *Drugs*. 2023;83(7):569–76.
114. Gehlot P, Pathak R, Kumar S, Choudhary NK, Vyas VK. A review on synthetic inhibitors of dual-specific tyrosine phosphorylation-regulated kinase 1A (DYRK1A) for the treatment of Alzheimer's disease (AD). *Bioorg Med Chem*. 2024;113:117925.
115. Chandra P, Sharma H. Phosphodiesterase inhibitors for treatment of Alzheimer's disease. *Indian Drugs*. 2024;61:7.
116. Sharma H, Chandra P, Verma A, Pandey S, Kumar P, Singh A. Therapeutic approaches of nutraceuticals in the prevention of Alzheimer's disease. *J Food Biochem*. 2023;46(12):e14426.
117. Zhu S, Stein Richard A, Yoshioka C, Lee C-H, Goehring A, McHaourab Hassane S, Gouaux E. Mechanism of NMDA receptor Inhibition and activation. *Cell*. 2016;165(3):704–14.
118. Wang Y, Tong Q, Ma SR, Zhao ZX, Pan LB, Cong L, Han P, Peng R, Yu H, Lin Y, et al. Oral Berberine improves brain dopa/dopamine levels to ameliorate Parkinson's disease by regulating gut microbiota. *Signal Transduct Target Ther*. 2021;6(1):77.
119. Feldman EL, Goutman SA, Petri S, Mazzini L, Savelieff MG, Shaw PJ, Sobue G. Amyotrophic lateral sclerosis. *Lancet*. 2022;400(10360):1363–80.
120. Christoforidou E, Joilin G, Hafezparast M. Potential of activated microglia as a source of dysregulated extracellular MicroRNAs contributing to neurodegeneration in amyotrophic lateral sclerosis. *J Neuroinflammation*. 2020;17(1):135.
121. Himanshu S, Monika K, Priyanka G, Sanakattula S, Ananya C, Sumel A, Radheshyam P. Role of MiRNAs in brain development. *MicroRNA*. 2024;13(2):96–109.
122. Kam TI, Hinkle JT, Dawson TM, Dawson VL. Microglia and astrocyte dysfunction in Parkinson's disease. *Neurobiol Dis*. 2020;144:105028.

### Publisher's note

Springer Nature remains neutral with regard to jurisdictional claims in published maps and institutional affiliations.